broad or strong emission lines in the optical-UV spectrum. By selecting radio sources in the optical SDSS database, only a $\sim 10\%$ of the objects shows a clear signature of nuclear activity, although in some of these objects a mild trace of non-thermal emission can be detected by using HST spectra (Chiaberge et al. 2003).

Combined studies of the 2dF survey with a southern radio survey (Sadler et al. 2002) and of the SDSS sources with the FIRST database (Ivezić et al. 2002) revealed that over 60% of the radio-loud galaxies in the nearby universe, despite hosting compact central radio sources and being confirmed to also have high X-ray to optical flux ratio, do not show any clear signature of AGN activity in the optical wavelength range and can be therefore defined "optically quiet" (Kollgaard et al. 1995; Fiore et al. 2000; Mushotzky et al. 2000; Barger et al. 2001; Giacconi et al. 2001; Mushotzky 2004). These sources would have never been discovered with optical surveys; similarly, a comparable percentage of the AGN population at higher redshifts does not show any measurable X-ray emission (Cowie et al. 2004).

The observed strong anti-correlation between the radio and the mid-IR flux in star forming galaxies can provide an additional tool to detect AGN by exclusion (Yun et al. 2001): low mid-IR to radio flux ratios often indicate AGN activity, while high ratios often correspond to starburst (Condon et al. 1995; Miller & Owen 2001). Condon et al. (1998) used this technique to flag as AGN some sources previously thought to be starbursts in the ROSAT All-Sky Survey.

In addition, Ivezić et al. (2002) used a sample of radio-selected sources from the SDSS database to show that, despite suffering from a large contamination, deep radio surveys appear to be often contaminated by quiescent galaxies but simultaneously allow to discover a large population of otherwise undetectable active nuclei.

3.2.2 IR selection

The search for AGN through IR selection started in the early 70's with the first high sensitivity IR detectors. The purpose is in this waveband to identify highly obscured nuclei activity by reprocessed dust emission.

The first large program, with IRAS (*Infrared Astronomical Satellite*), identified AGN by

60 μm to 25 μm luminosity ratio, found to deviate from common values in quiescent galaxies (Spinoglio & Malkan 1989).

Many years later, Laurent et al. (2000) derived by ISO data for low redshift AGN that also the 12 μm to 18 μm and the 5 μm to 8.5 μm colors were useful AGN indicators.

Moreover, optically selected active nuclei generally showed a mid-IR (from 3 to 10 μm) excess when compared to normal galaxies. Mid-IR luminosity also appears to be tightly correlated to the bolometric luminosity in known AGN, with small intrinsic scatter (Andreani et al. 2003), thus providing a proxy to the overall nuclear emission without any need for a complete SED characterization.

The 2MASS (*Two Micron All Sky Survey*), in the late '90s, revealed that $\sim 60\%$ of the IR selected objects with $J-R > 2$ have AGN as their optical counterparts. The contamination is mostly due to heated dust in star forming regions and can only be avoided with a broad band photometric follow up (from 4 to ~ 100 μm). In order to disentangle AGN and starburst contributions, the spectroscopic features by PAH (*Polycyclic Aromatic Hydrocarbon*) molecules also provide powerful help: in particular, the absence of broad 7.7 μm and 3.3 μm emission lines is an indicator of AGN activity, since the highly ionizing AGN continuum is thought to destroy PAH molecules.

On the other hand AGN usually show an hydrocarbon dust grains absorption line at 3.4 μm (Risaliti et al. 2003).

With the advent of Spitzer and, later, Herschel, IR surveys offered new powerful opportunities to unveil large samples of highly obscured Compton thick AGN, that were missing in X-ray surveys. Again, the mid-IR excess, compared to the expected emission by stars based on the observed star formation rates, is considered a standard parameter for AGN identification, since even in the most obscured active nuclei the primary radiation has to result in a corresponding thermally reprocessed radiation by the intercepting material. To date, mid-IR selected AGN inside star-forming galaxies at $z \sim 2$ are thought to contribute with a 10-25% to the missing X-ray background between 10 and 30 keV, and most of XRB still to be resolved is likely to be ascribed to similar sources at $z \lesssim 1.4$ (Gilli et al. 2007; Daddi et al. 2007).

3.2.3 Optical and UV selection

The selection of AGN via their optical and UV spectral features has its origins in the very first definition of nuclear activity itself by the observation of broad emission lines in Seyfert galaxies. The elaboration of a complete selection machinery by using AGN' deviation from integrated stellar emission of the host galaxy was provided by Schmidt (1969) and Sandage 1971. AGN candidates detection was triggered by matching any of the following criteria: non thermal colors at any redshift, a point-like source without proper motion or a Seyfert-like radial surface brightness distribution, rapid time variability, broad permitted and narrow forbidden high-ionisation emission lines. The candidates were then confirmed by a follow up with high resolution optical spectroscopy, radio and/or X-ray observations. By these means, it is clear that AGN optical surveys were initially heavily biased towards Type 1 (i.e., broad-line) AGN. It is indeed very difficult to find AGN with intrinsic low luminosity even at low redshifts: the stellar integrated emission dilutes the AGN signature in the overall observed spectral energy distribution of the galaxies and there is no clear correlation between AGN and host galaxy bolometric luminosity (Urry 2003).

The craved completeness of the samples can only be approached with sophisticated color selection techniques. In the SDSS surveys, for example, the candidates are picked out from a five colors parameter space (Fan et al. 1999; Richards et al. 2004; Richards et al. 2009) and triggering thresholds are calibrated on well known active nuclei. In this case, the wavebands are u(0.35 μm), g(0.48 μm), r(0.62 μm), i(0.76 μm) and z(0.91 μm). The survey claims to reach a completeness above 90% and a flux limited detection. It is nevertheless the case to underline that even the SDSS fails in detecting optical counterparts of large samples of X-ray sources discovered with XMM-Newton or Chandra.

Moreover, all the survey in the optical waveband suffer of potential heavy contamination by starbursts. It is emblematic the case of the Byurakan surveys: with a contamination fraction of $\sim$ 90% they turned to be starburst - and not AGN - surveys.

Also the line suppression by dust and gas clouds along the line of sight should be taken into account as possible obstacles to get complete optical samples. In this case, a near-IR follow

up can help to uncover reprocessed nuclear activity, but a reliable average reddening curve in active nuclei has still to be derived in order to compute corrected optical fluxes, since it appears to consistently differ from the one originated by the interstellar medium in MW (Maiolino et al. 2001).

Other selection methods in the optical waveband can refer to high variability (Boutsia et al. 2009, 2010; MacLeod et al. 2011; Graham et al. 2014). As already mentioned the main issue is in this case given by the large observing time required. Nevertheless, this technique can also lead to a relevant fraction of false positive detections made up by variable stars and supernovae. Variability surveys have therefore to be combined with other selection criteria.

3.2.4 X-ray and high energy selection

Like for radio surveys, AGN detections in the X-ray and Gamma-ray waveband have virtually no false positives, since almost every high latitude, compact X-ray or Gamma-ray source is an active galactic nucleus. These surveys provide therefore AGN samples without any need for confirmation by follow up in other bands. Recent observations also have S/N ratios high enough to let us derive redshifts and the initial positional accuracy issues have been solved with the advent of XMM-Newton and Chandra, with resolutions of mirror PSF FWHM of 6" and 0.2", respectively. The recent improvements also permit to take advantage of the possibility of the X-rays to investigate the innermost regions of the AGN, since they are produced very close to the black holes.

It should also be noted that at any fixed optical magnitude no other waveband can provide as many AGN detections as X-rays (e.g. Chandra finds on average $\sim 1000\,\mathrm{deg}^{-2}$ at $r < 24$ with a flux limit of $F_X(0.5-2\ \mathrm{keV}) = 5 \times 10^{-16}\,\mathrm{erg\ cm^{-2}\ s^{-1}}$). Hard X-rays also offer a threshold for certain AGN detection: above $L_{2-10\ \mathrm{keV}} > 10^{42}$ erg s^{-1} there are no false positives. The faintest fluxes, on the other hand, also permit to define a lower limit to nuclear activity: below fluxes of $\sim 10^{-16}$ erg s^{-1} cm^{-2} in the range $2-10\,\mathrm{keV}$ the ratio between AGN and quiescent galaxies rapidly drops (Hornschemeier et al. 2003).

While optical and UV surveys suffer from starlight contamination (especially from young massive stars), IR survey also detect dust from star forming regions and radio observations

are heavily affected by false positives due to HII regions, supernovæ and rapid star formation, X-rays do not show such limitations. The high detection efficiencies of X-ray surveys is given by two concomitant factors: the high sensitivity achieved by current instruments and the high penetrating power of X-ray, which let us unveil nuclear activity even in highly obscured sources, completely missed by optical surveys. Column densities of the order of $N_H \lesssim 3 \cdot 10^{23}$ cm^{-2} do not affect significantly the measured flux at $E > 5$ keV.

Thanks to X-ray, Gamma, radio and IR surveys it has been possible to quantify the fraction of obscured active nuclei: the dilution of optical and infrared brightness due to starlight has no effects on sources with bolometric luminosities above 10^{41} erg s^{-1} and on radio sources with power per unit frequency above 10^{41} W Hz^{-1}. Most AGN have thus been discovered to have large column densities, with $N_H > 10^{22}$ cm^{-2}.

The obscuring material intercepting the continuum from the accretion disk has mostly to be identified with the dusty torus surrounding a black hole and deeply affects the out-coming X-ray flux by Compton scattering processes. The optical depth for Compton scattering $\tau = N_H \sigma_T$ defines therefore three subsets of objects: the sources with $\tau \ll 1$ are Compton thin and are efficiently detected in X-ray surveys without any significant suppression; the sources with $\tau \sim 1$ are Compton-thick AGN with a significant dimming of the spectrum below 10 keV and are efficiently detected only by hard X-ray surveys, such as Swift/BAT or Integral/IBIS; the sources with $\tau \gg 1$ are heavily Compton thick sources whose nature can only be revealed by auxiliary methods, such as a strong iron Kα line emission over a flat X-ray continuum at low energies (Comastri et al. 2011; Feruglio et al. 2011; Iwasawa et al. 2012a,b; Vignali et al. 2014).

The study of heavily obscured sources is not only important for a complete census of the AGN population: every BH-galaxy interaction scenario predict a phase of intense inflows of matter onto the black holes and simultaneous high star formation rates in the host galaxy, mostly triggered by mergers. These inflow phases can only be revealed by X-ray observation and represent the missing link between quiescent and AGN phases, when a self-regulating emission sweeps the most part of diffuse dust and gas, thus quenching star formation and establishing the BH-galaxy relations. This latter phase is confirmed by recent observations

of molecular outflows in quasars hosted in ULIRGs also in high redshift sources (Maiolino et al. 2012), by the detection of outflows in neutral and ionized gas (see e.g. Alexander et al. 2010 and Harrison et al. 2012), and by X-ray emission by highly relativistic winds (Tombesi et al. 2012).

The wide X-ray band can be divided into three main subranges: the soft X-rays (with energies between 0.2 and 2 keV), the hard X-rays (from 2 up to 6 keV) and the very hard X-rays (from 5 to 10 keV). Each subrange is characterised by significant differences in AGN selection: soft X-ray surveys (such those carried out with Einstein and ROSAT) mostly find broad line quasars and narrow line Seyfert 2 galaxies and suffer from extinction effects just like the optical and UV ones; hard X-ray surveys (like ASCA and BeppoSAX before and XMM-Newton and Chandra after) also detect AGN with no spectral features in the optical-UV range. On the whole, $\sim 30\%$ of the X-ray sources appear to have optical counterparts in broad line AGN, while the remaining $\sim 70\%$ correspond to objects with strong absorption lines, often almost invisible even to HST. The latest define the class of the "optically-dull" AGN (Elvis et al. 1981).

To summarize, at high luminosities optical and X-ray surveys are equally sensitive, while at low luminosities X-ray unveil a larger number of sources, also detecting objects which are optically dimmed due to dilution by starlight, dust and gas absorption. The surveys in the optical waveband have the undeniable advantage to provide a spectroscopic signature of broad line emission that can be used to infer large samples of accurate SMBHs mass measurements through SE observations and the radius-luminosity relation. Moreover, a detailed and careful characterisation of the spectra can let us quantify the effect of radiation pressure and outflows on the AGN and host galaxy structure and evolution.

Part of the present work is thus dedicated to examine the state of the art of optical data provided by the SDSS, trying to ameliorate the available spectral decomposition. In this regard, it should always be remembered that the inferred conclusions derived from the SDSS come with all the intrinsic biases of the survey (Shen et al. 2008).

3.3 The Sloan Digital Sky Survey

The large project of the Sloan Digital Sky Survey (SDSS) started its operative phase in year 2000 (York et al. 2000) and will start its 4th phase with its 12th Data Release (DR) in the next February 2015. The next DR will also be the first to include observations from the Southern Hemisphere, provided by the Irénée du Pont Telescope at Las Campanas Observatory.
In this Section I will briefly summarize the main purposes of the SDSS, without any claim of completeness. For comprehensive description of the instruments and the scientific goals of the SDSS-I/II/III surveys we refer anyway to the SDSS website[1] and to the specific Data Release papers (Abazajian et al. 2009 for the DR7 and Ahn et al. 2014 for the DR10).
This work will examine the available data up to now, taken with the Sloan Foundation 2.5m Telescope (Gunn et al. 2006) at Apache Point Observatory, in south east New Mexico (Latitude 32°46′49.30″ N, Longitude 105°49′13.50″ W, Elevation 2788m). The telescope has a modified two-corrector Ritchey-Chrétien design, with a 2.5m primary mirror a 1.08 m secondary mirror and a final focal ratio of approximately f/5. The 3° distortion-free FOV is also guaranteed by an astigmatism corrector and two aspheric correctors in close proximity to the focal plane.
The incoming light is conveyed on a camera or a spectroscopic plate, depending on the planned observation. The camera is array of 6 columns each containing five 2048x2048 SITe/Tektronix CCDs (see Figure 3.1). The telescope is designed to work in a drift scan mode: it moves along precise circles on the sky at the sidereal rate so that a specific object produces an image along an entire column of pixels, which are parallel to the scan direction. The image is then read at the same rate the light is collected. Each row corresponds to a different filter of the SDSS *r* (6166 Å), *i* (7480 Å), *u* (3551 Å), *z* (8932 Å), *g* (4686 Å) colour space and produces an image in a 54 seconds exposure time. By taking into account the necessary separation between the mosaic rows, each object requires a 2-pass observation of $\sim 340\,\mathrm{s}$ exposure time to produce a complete 5 colour image set. The response curves of each colour filter have been measured by Gunn et al. (1998) (see Figure 3.2) and have been

[1] `http://www.sdss3.org/collaboration/description.pdf` and references therein.

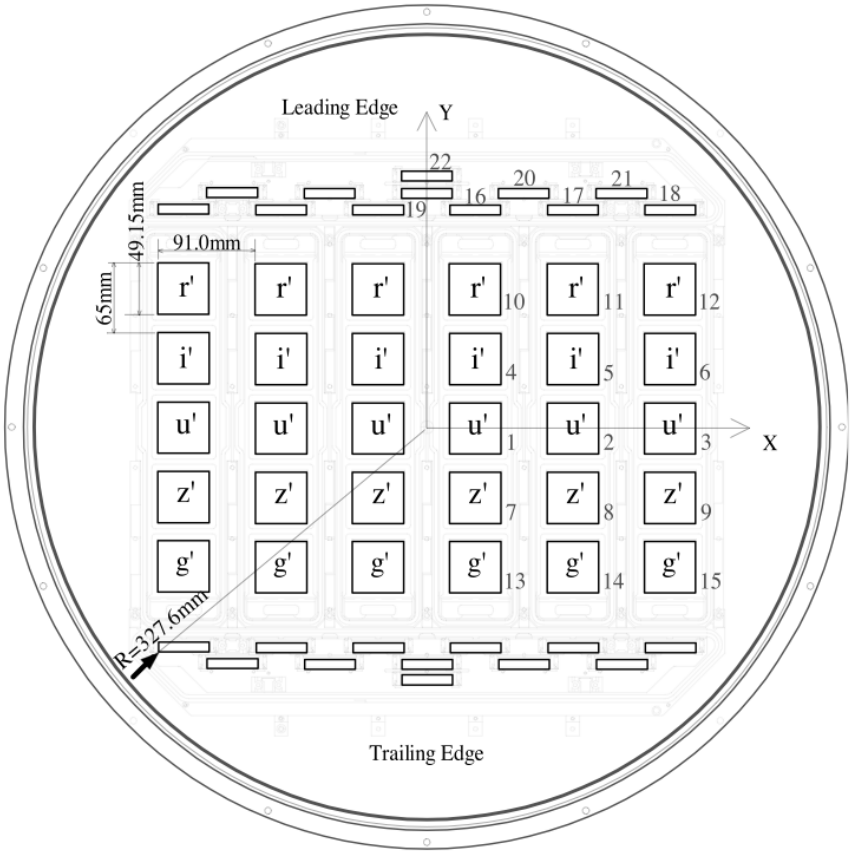

Figure 3.1 Optical layout of the focal plane of the SDSS camera.

corrected by later estimates (Doi et al. 2010). Additional 24 CCDs are dedicated to derive astrometric data.

During the first two project phases (2000-2008) there have been seven Data Releases, the latest of which includes over 347 million objects in a wide scanned area of $11\,663\,\mathrm{deg}^2$. The DR7 imaging database consists of three different surveys with completely different purposes: the Sloan Extension for Galactic Understanding and Exploration (SEGUE) catalogue, with its 127 million distinct sources, aimed at investigating the structure, kinematics and taxonomy of the stellar population in our own galaxy. $\sim 240\,000$ stars of this survey have been chosen for a spectroscopic follow up. The Legacy survey, instead, includes 230 million objects and was designed to detect and provide accurate positions for a spectroscopic follow up of almost 10^6 galaxies and $\sim 120\,000$ quasars in the wavelength range $3\,800-9\,200$ Å with a spectral resolution in the range $\lambda/\Delta\lambda \in [1800, 2000]$, in order to study the large scale

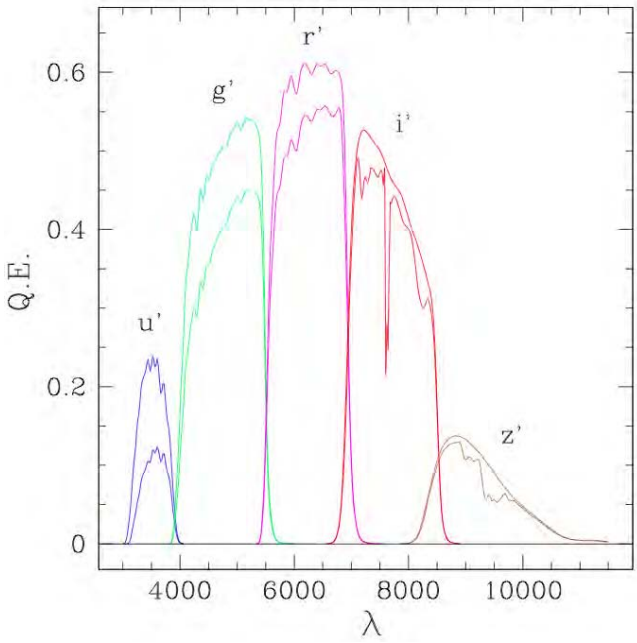

Figure 3.2 Quantum efficiency for each filter in the SDSS photometric array. Lower curves for each filter include the effects of atmospheric extinction for 1.2 air masses at local site.

structure and evolution of the universe. A third subset of imaging data included in the DR7 is given by the Supernova Survey, consisting in a repeated scanning of the SDSS Southern equatorial stripe 82, in order to detect new SNæ($\sim$ 500 have been found) and measure their lightcurves.

During the SDSS-III phase (2008-2014), several new projects joined the pre-existing ones. The Multi-object APO Radial Velocity Exoplanet Large-area Survey (MARVELS) was designed to measure the radial velocity curves of $\sim$ 10000 main sequence stars and $\sim$ 1000 giants in order to unveil the presence of gas giant planets in their proximity. The Apache Point Observatory Galactic Evolution Experiment (APOGEE), instead, provided IR spectra for 100000 red giant stars, with a dedicated high resolution, cryogenic spectrograph, in order to give new perspectives on MW history and support near-field cosmology tests of galaxy formation and dark matter distribution. A second phase of the SEGUE survey extended the coverage of the previous dataset, while the Baryon Oscillation Spectroscopic Survey (BOSS) succeeded the Legacy Survey in collecting galaxies and quasars position, redshifts, photometric data and spectra.

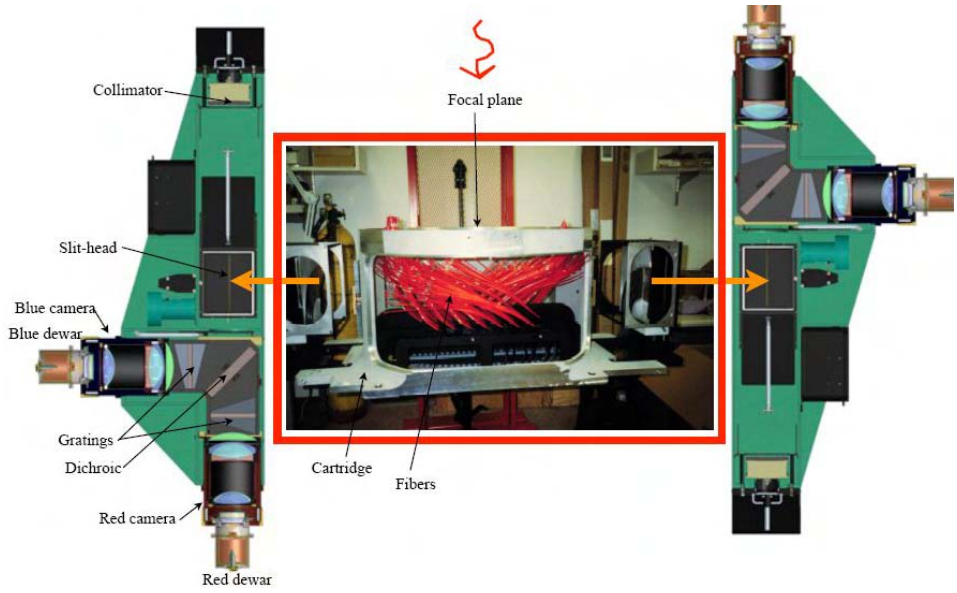

Figure 3.3 Optical setup of the SDSS-BOSS spectrograph.

With the SDSS-III phase the Sloan produced the last available dataset, the DR10. In particular, a major upgrade for extragalactic observations is given by the introduction of the new BOSS spectrograph (see Figure 3.3), whose primary purpose is given by the measurement of the baryon acoustic oscillation feature (BAO, see Peebles & Yu 1970; Sunyaev & Zeldovich 1970) in the clustering of galaxies and the Lyman-α forest.

The BOSS program has already provided 684 000 new optical spectra in the wavelength range $3\,600-10\,400$ Å at a resolution in the range $\lambda/\Delta\lambda \in [1400, 2600]$, and more have to come: the final goal of the survey will include more than 1.5 million galaxy spectra up to $z \sim 0.7$ and 160 000 quasar spectra with redshifts in the range $2.2-3.5$, implementing a new series of pipelines[2].

The collective coverage of the first 10 Data Releases is of $14\,555\,\mathrm{deg}^2$ for the imaging data. As for the spectroscopic dataset, the SDSS spectrograph provided a $9\,274\,\mathrm{deg}^2$ coverage, while the BOSS spectrograph will cover $6\,373\,\mathrm{deg}^2$ (see Figure 3.4).

The outstanding number of spectra that the SDSS has been able to provide in this last few years is due to the capability of the spectrograph to produce several hundreds of spectra for each single exposure (640 for SDSS-I/II spectrograph and 1000 for BOSS spectrograph

[2] http://www.sdss3.org/dr10/algorithms

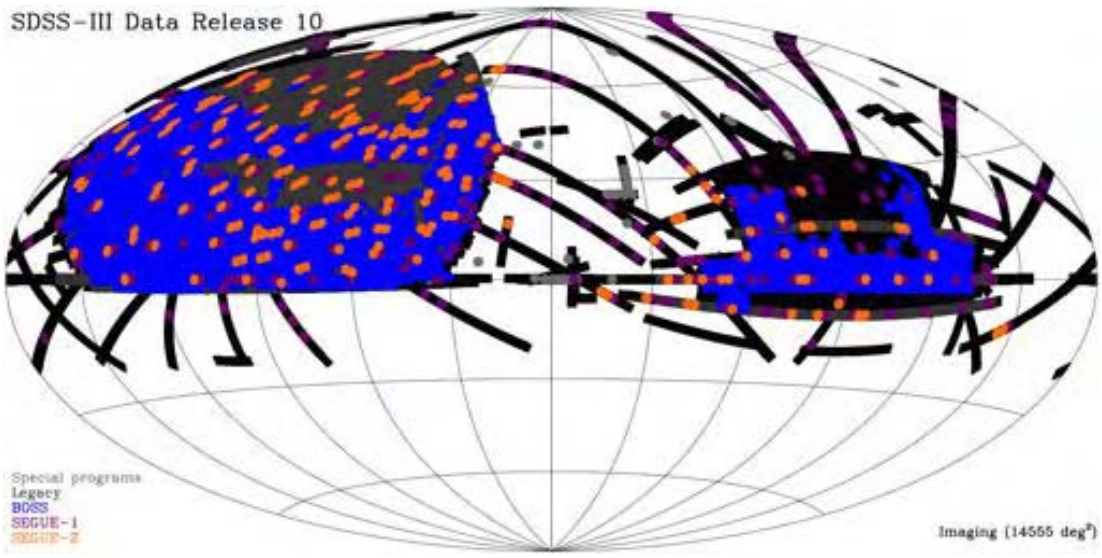

Figure 3.4 Sky coverage of the SDSS-BOSS Data Release 10.

respectively). As already mentioned above, the photometric data is used to select the interesting objects. The position of these objects is then used to accurately design single aluminium spectrometric plates for each FOV. Each source corresponds to a little hole drilled in the plate, which subtends in turn a solid angle of 3″ (for SDSS-I/II) or 2″ (for BOSS). Each hole has to be plugged with an optical fiber connected to the spectrograph. The light is then guided to a beamsplitter which separates at roughly 6000 Å the blue part of the spectrum from the red one. The two ranges are recorded on separate CCDs with optimised quantum efficiency for that particular waveband.

Each spectrum is then recomposed and calibrated by a processing pipeline and identified by the modified Julian date of the observation (MJD tag in the catalogue), its plate number and fiber identification number (PLATE and FIBERID tags in the catalogue).

3.4 The DR7 and DR10 Quasar catalogues

The second and the third phase in the SDSS project produced 2 spectroscopic catalogues of quasars: the first one (DR7Q, in the following) was published after the DR7 by Schneider et al. (2010), while the latest (DR10Q) after DR10 by Pâris et al. (2014).

DR7Q already contained 105 783 *bona fide* quasars, with magnitude $M_i \leq -22.0$ and having at least one broad emission line with $FWHM \geq 1000$ km s^{-1} and also included the BAL quasar catalog by Gibson et al. (2009). The selection has been performed using several different procedures: $\sim 50\%$ of sources are uniformly selected using Richards et al. (2002) algorithm, while the remaining ones derive from selection criteria described in Schneider et al. (2010). The catalogue is still available at its website[3]. A later spectral characterization of this sample, provided by Shen et al. (2011)[4], will be extensively discussed in the following. DR10Q includes 166 583 objects, with multiple candidates selection criteria fully described in Pâris et al. (2014). The quasars of the DR7Q database included in the sample are flagged as previously detected: in particular, all the quasars with $z \geq 1.8$ have been reobserved to take advantage of the improved throughput of the BOSS spectrographs. The initial 321 729 candidates flagged as quasars by the SDSS-BOSS new pipeline has then entered a visual confirmation phase, providing the final parent sample, with objects from redshift $z = 0.053$ up to 5.855. The catalogue is now available at its dedicated public website[5], which also provides a summary and a description of the data contained in each column.

3.5 The state of the art in spectral fitting of quasar spectra

Several attempts have been made in the past years to retrieve statistical informations about the structure, composition and emission properties of the AGN from the shape and features of the optical-UV spectrum (e.g Boroson & Green 1992; McLure & Dunlop 2004; Shen et al. 2008, 2009). In particular, as already mentioned in Chapter 1, the broad emission lines have been used to calibrate virial black hole masses and derive black hole mass functions, while the continuum can be used to infer AGN luminosity functions. Both can give informations about the interaction of the AGN with the host galaxies and the processes that originate the BH-galaxy correlations. It is important to remember once more that statistically affordable results can only derive from uniformly selected samples of sources (see e.g. Richards et al.

[3] http://classic.sdss.org/dr7/products/value_added/qsocat_dr7.html
[4] http://users.obs.carnegiescience.edu/yshen/BH_mass/data/catalogs/
[5] http://www.sdss3.org/dr10/algorithms/qso_catalog.php

2002 for uniform selection algorithm of SDSS DR7 quasars).

In this Section I will briefly discuss the state of the art in spectral fitting of broad line AGN as presented by Shen et al. (2008, 2011), while in the next Section we will describe an improved analysis that provides more accurate results.

The Hα, Hβ, Mg II and C IV broad emission lines are certainly the most interesting ones in the optical-UV spectrum, not only because they are almost always resolved with a good signal to noise ratio, but especially for their being used as SMBH virial mass estimators (e.g.Vestergaard & Peterson 2006; Vestergaard & Osmer 2009). In Chapter 2 we have confirmed the importance of Hβ and Mg II lines, in particular, by showing how they provide better constrains on SMBH mass, with respect to C IV broad emission line, since they are less sensitive on the internal geometrical structure of the BLR. This results in a lower intrinsic dispersion of the BLR mean emissivity radii versus continuum luminosity relations. We will then focus on these emission lines.

Continuum and Iron emission

In Shen et al. (2011), a preliminary phase in spectral fitting consists in correcting for galactic extinction by using the Schlegel et al. (1998) map and the Milky Way extinction curve from Cardelli et al. (1989) and shifting the spectra to rest-frame using the cataloged redshifts. Rest-frame spectra can then access to the continuum and iron emission subtraction, through a 5 parameter fitting: 2 degrees of freedom (amplitude and slope) are given by the continuum emission, which is represented by a power-law. The FeII spectrum is on the other hand represented by a specific template (which is discussed in the following) that is conveniently broadened, shifted in its systemic velocity and adjusted in amplitude to match the spectrum at its best. Both continuum and iron parameters are fitted in a wavelength regions that are obviously close to a specific emission line but lays outside its broad wings. In the case of Hα, these fitting windows are given by the wavelength ranges $[6000;6250]\cup[6800;7000]$ Å, while for Hβ, Mg II and C IV they are $[4435;4700]\cup[5100;5535]$ Å, $[2200;2700]\cup[2900;3090]$ Å and $[1445;1465]\cup[1700;1705]$ Å, respectively. The chosen template for the iron emission is not the same for the four considered

emission lines: for Hα and Hβ the Boroson & Green (1992) template has been found to give the best results, while for the Mg II broad line the iron emission is fitted with the Vestergaard & Wilkes (2001) template. The two adopted templates are both derived from the observed spectra of I ZW 1, the prototypical narrow-line Seyfert 1 galaxy. Boroson & Green (1992), in particular, provide a template in the wavelength range 4250 Å $\leq \lambda \leq$ 7000 Å, while Vestergaard & Wilkes (2001) provide the empirical separated FeII and FeIII UV templates in the wavelength range 1250 Å $\leq \lambda \leq$ 3080 Å. At wavelengths around the 1549 Å of C IV, the iron emission component is too weak to be sufficiently constrained in the SDSS low signal to noise spectra, thus is not fitted at all.

Broad line emission

Each broad line is fitted in a wavelength range broad enough to entirely include its wings and other strong emission features in the neighbourhoods. The Hα fitting range is set in Shen et al. (2011) to [6400; 6800]Å; for the Hβ region is [4700; 5100]Å, for Mg II is [2700; 2900]Å and, finally, for C IV the fitting region is set to [1500; 1600]Å.
Each broad line fitting is then performed both with a single Gaussian and with a multiple set of 2 or 3 independent Gaussians all having a FWHM lower limit of 1200 km s^{-1}, consistently with Baskin & Laor (2005) and Fine et al. (2006).

Narrow line emission

Each broad emission line is considered to also have an underlying narrow component arising from NLR clouds. This feature is fitted in Shen et al. (2011) by a single Gaussian with three free parameters: its amplitude, its velocity offset with respect to the redshift z and its Doppler broadening.
In the particular case of Mg II, since the authors claim it is not clear whether it is always present a strong narrow component, the fit is executed both with a single broad Gaussian (in order to use e.g. McLure & Dunlop 2004 calibration for BH virial masses) and with multiple broad and single narrow Gaussian components (according to Vestergaard & Osmer 2009 method for virial masses calibration).

It happens, in the Hα and in the Hβ wavelength ranges, to also have other strong narrow emission features in the neighbourhoods. In the Hα region, for example, we can recognise the [N II]6548,6584Å and the [S II]6717,6731Å doublets. Each doublet is represented by a couple of single Gaussian lines, whose velocity offsets from systemic redshift and line widths are imposed to be the same. In the case of the [N II] doublet the two amplitudes are forced to have a ratio of 2.96, according to theoretical predictions.
In the Hβ region, the [O III]4959,5007Å doublet is fitted with two Gaussians for each line of the doublet with free width and amplitude, in order to reproduce their frequent blue winged or double peak profiles. The two components of each line are also forced to have the same FWHM and velocity offset.

3.6 A new machinery in quasar spectral fitting

As already mentioned above, the analysis of optical-UV emission features and their spectral decomposition with accurate line profile is not only fundamental in order to estimate reliable BH masses, but also to reveal the effects of radiation pressure and outflows taking place over the whole AGN accretion and emission phase. Quasar spectroscopy can therefore provide unique tests to identify the physical processes responsible for BH-galaxy coevolution.
The effects of radiation pressure and outflows can obviously be observed in non-Gaussian line profiles and quantified with their high- and low-velocity wings. A very accurate characterisation of broad lines can also provide correct FWHM estimations to be used in BH mass measurements. To this end, it is important to remember that viral BH estimates can only be inferred by using broad line FWHMs that have been obtained with a coherent fitting method adopted for the determination of the RM parameters, otherwise a new calibration becomes mandatory.
A correct spectral decomposition has nevertheless to reflect a plausible emission process, the adopted physical geometry and internal structure of the emitting region. Therefore we considered worthwhile improving, in particular, the interpretation and modelling technique of the underlying iron template and of the broad lines profiles. With respect to Shen et al.

(2009) and Shen et al. (2011) approach, we preferred indeed not to use average templates for the iron emission lines but to derive their contribution on every single spectrum by fitting a suitable combination of iron templates obtained from CLOUDY models in a wide range of physical conditions. Moreover, at variance with Shen et al., we fit at the same time the emission lines, continuum and the iron emission. Finally, we tried as much as possible to fit broad lines with a single line shape instead of using multiple Gaussian lines. Apart for using a lower number of free parameters, such approach produces more stable fit results.
In the next paragraphs I will describe in detail our choices for line fitting profiles and their relative free parameters. At the end of this Chapter, I will present the results achieved with this new approach and compare them with the previous analysis by Shen et al.

3.6.1 QSO selection

The sample we use for testing our fitting method is directly derived from SDSS DR7 Schneider et al. (2010) quasar catalog, updated with all the SDSS DR10 sources which have been either targeted or classified as a QSO by Pâris et al. (2014) . All the DR7 spectra come with observed wavelengths in the range [3800;9200], while DR10 spectra have a wavelength coverage of [3650;10400]. From this parent sample, containing 105 783 and 166 583 *bona fide* quasars from DR7 and DR10 respectively, we extract the sources with photometric redshift below 0.8, in order to select only the quasars with an [O III] line in the observable wavelength range, consistently with Risaliti et al. (2011). We also rule out all the quasars which have been flagged by the standard SDSS pipeline as sources with high uncertainty in redshift determination (i.e. the sources with `ZWARNING` = 1).
From the obtained subset, we compute spectral fitting in the two separate regions of Hβ (including He II 4687,4861Å and the [O III] doublet) and Mg II. In particular, for consistency with Shen et al. (2011), we fitted the continuum and iron emission in the ranges [4435;5535] for Hβ and [2200;3090] for MgII. This leads in the end to 14347+13538 Hβ spectra (from DR7 sources with $z \in [0;0.66]$ and DR10 sources with $z \in [0;0.8]$, respectively) and 2798+11325 Mg II spectra (from DR7 sources with $z \in [0.73;0.8]$ and DR10 sources with $z \in [0.66;0.8]$, respectively). No thresholds are imposed for the signal to noise

ratio.

3.6.2 Spectral fitting of DR10 quasars

For a direct comparison with the results available in the literature, we consider for the iron and continuum emission the same fitting ranges of Shen et al. (2011). Within these ranges, particular attention is dedicated to excluding all the wavelength channels which should not be considered affordable. To this end we use the available SDSS spectra and its associated error arrays, ruling out infinite values, which can cause convergence problems during the automatic fitting procedure. Moreover, we use the SDSS image layers to exclude all the pixels coming with mask bits set to `FULLREJECT`, `NOSKY`, `NODATA`, or `BRIGHTSKY`. The obtained masked spectra are then ready for the automatic fitting procedure, which is performed over the whole spectral range by including all the components at the same time and not with a preliminary continuum and iron template fitting in very narrow wavelength windows (like in Shen et al. 2011).

The non-linear least squares fitting is obtained by using the `IDL MPFIT` procedure[6] (for an exaustive discussion see Markwardt 2009). In order to avoid the possiblity to get results by a local minimum of the estimators, we perform a 3-pass fitting: at first, the spectral fitting procedure uses just reasonable starting points for each parameter, while, for the following iterations, we set the starting points to the results of parameter fitting of the previous step. A tolerance in each parameter determination is set to 10^{-5}.

Continuum emission

The emission from the accretion disk in the optical-UV waveband is modelled with a power-law, as usual, with two free parameters: its amplitude and slope. The normalization of the power-law is defined by a reference wavelength λ_{ref} for each fitting range: in the Hβ region, we set λ_{ref} to 5100Å, while in Mg II range λ_{ref} = 3000 Å. The slope is constrained to lay within the reasonable limits of [-2;2], which are consistent with the observations: for example, from an homogeneous data set of $\sim$ 2200 SDSS quasar spectra Vanden Berk et al.

[6] `http://purl.com/net/mpfit`

(2001) derive a spectral index of $\alpha_\nu = -0.44$ in the wavelength range 1300 Å $\leq \lambda \leq$ 5000 Å (see also e.g. Telfer et al. 2002 and Risaliti & Elvis 2004).

Iron emission

In order to find the best way to fit the Iron emission, several attempts have been done both by using observed templates averaged over large QSO samples (Tsuzuki et al. 2006; Véron-Cetty et al. 2004; Vestergaard & Wilkes 2001). Finally we opted for a more coherent framework, in which the iron emission is derived by using locally optimally emitting clouds models, similar to the ones we adopted to describe BLR internal structure. Iron emission is therefore obtained by using 20 independent CLOUDY (C13) models with electron density ranging between 10^8 and 10^{14} cm^{-3}, a incident flux within 10^{17} and 10^{23} erg s^{-1} cm^{-2} both with and without internal turbolence of ~ 100 km/h. From each photoionization calculation we derive a template that represents the *theorical* iron emission from one single cloud in that specific physical condition. What is indeed observed is substantially different: the theoretical emission has to be convolved with a line profile and combined with all the other emission spectra of the other clouds with similar incident flux and electron density. These clouds are obviously in relative motion along non-coplanar orbits around the SMBH and are also subject to eventual outflows/inflows and radiation pressure effects. The overall template profile is finally observed as projected along the line of sight.

With our fitting procedure we tested whether a naïve convolution of the template with a single Gaussian (also used, e.g., in Shen et al. 2011) is able or not to account for all these effects with a sufficient accuracy. To this end, in agreement with van der Marel & Franx (1993), we represent the order zero of the spreading of a line profile with a gaussian with a mean velocity v_0 and a velocity dispersion σ

$$\mathscr{L}_0(v) = \frac{1}{\sqrt{2\pi}\sigma} \exp^{-1/2(v-v_0)^2} \tag{3.1}$$

and reproduce the corrections to this trivial assumption up to an order $N = 3$ by using the orthonormal Gauss-Hermite polinomials $H_j(v - v_0)$. We convolve therefore our theoretical

iron template with a line-of-sight velocity distribution (LOSVD) $\mathscr{L}(v)$ given by

$$\mathscr{L}(v) = \mathscr{L}_0(v) \cdot \sum_{j=0}^{N} h_j H_j(v - v_0) \tag{3.2}$$

which has therefore, in our case, 6 free parameters (v_0, σ, h_j). The result is then normalized to a certain amplitude parameter A and composed with the other analogous templates coming from all the other CLOUDY models and finally fitted to the QSO spectrum, by assuming that all the iron templates are convolved with the same $\mathscr{L}(v)$.

A visual inspection over a large sample of quasars confirmed that the spectral resolution and the generally low S/N ratio of the SDSS spectra is not sufficient to constrain the h_j parameters, thus the high order corrections to the convolution with a simple Gaussian can be easily neglected.

Line fitting in Hβ region

In the wavelength range between 4435Å and 5535Å we find the broad and narrow components of Hβ, the almost underlying He II4861Å feature, the He II4687Å emission line and the narrow lines of the [O III] doublet.

For the Hβ broad line we made several tests in order to determine the best line shape to be used in the automatic fitting procedure. We compared by visual inspection the fitting results with a single and a multiple Gaussian lines, a Gauss-Hermite polinomial and a Lorentz function. In the end, it appears to be the best choice, in the vast majority of the cases, to use an asymmetric power law profile normalized to a parametrised amplitude and smoothed by a convolution with a single Gaussian. The adopted line profile model has therefore 5 free parameters.

The underlying He II4860Å feature is modelled in the same way, but leaving as a free parameter only its amplitude, thus forcing its velocity offset, power-law slopes and velocity dispersion σ to be the same of the Hβ broad component.

For the He II4687Å we use a simple gaussian (other additional 3 d.o.f.), while for the [O III] doublet, we tried to model each line with a single Gaussian profile. We reproduced the two

lines of the doublet, at 4959Å and 5007Å , respectively, with a fixed flux ratio of 1/3, in accordance with theoretical predictions and observations (Leisy & Dennefeld 1996; Galavis et al. 1997; Storey & Zeippen 2000; Dimitrijević et al. 2007). An additional Hβ single narrow gaussian has been added to the narrow template, with with only its flux as a free parameter. All the three lines of this template are assumed to have the same σ. In order to get even better fitting results we later decided to double this template, thus modelling each emission line with two single gaussians. This second template can vary in velocity offset and σ with respect to the first one, but has the same flux ratios between the lines, thus its amplitude is simply rescaled by the fitting procedure.

Line fitting in Mg II region

The Mg II feature is indeed produced by a doublet of two lines very close to each other, at 2796Å and 2803Å respectively. Their broad line emission is reproduced, in analogy with the Hβ broad lines, by a convolution of an asymmetric power-law profile with a smoothing gaussian, with 5 d.o.f. on the whole. The flux ratio of the two lines is set to 3/2 and velocity offsets, power-law slopes and velocity dispersion of the Gaussian convolution functions are assumed to be the same.

The narrow components are directly derived from the broad lines template described above, by simply using single narrow Gaussian lines instead of asymmetric power-law profiles, thus we have only three additional degrees due to the first line of the doublet and no other free parameters for the second line.

3.6.3 Results

In this Section we show a few plots of the results we obtained with our fitting method, which will be extensively applied in the next Chapter. We use the redshifts from the catalogue for the selection and as first guesses (see Figure 3.5 for a distribution over the whole sample) and estimated the S/N ratio over the whole broad line fitting wavelength range (Figure 3.6). SDSS spectra confirm to have a still low average signal to noise ratio, which makes it difficult

to constrain the fitting parameters. The final amount of fitting free parameters is, in our analysis, of 45 for the Hβ wavelength range (17 for the emission lines, 2 for the continuum and 26 only for the FeII emission) and 44 for the Mg II wavelength range (16 for the emission lines, 2 for the continuum and 26 only for the FeII emission). The fitting method adopted by Shen et al. (2011) requires instead 28 free parameters for the Hβ region (20 for the emission lines, 2 for the continuum and only 3 for the FeII template) and 20 free parameters for the Mg II region (12 for the lines, 2 for the continuum and 3 for the FeII template). We therefore reduced the number of parameters for the emission lines in the Hβ region and increased it in the Mg II wavelength range. We also notice that the overall number of free parameters is in our case much larger mostly due to our completely different way to model the FeII emission. When compared with Shen et al. (2011), our fitting method shows a better distribution for the reduced χ^2 (see Figure 3.7). Anyway, it is clear that Hβ spectra are much more noisy and difficult to reproduce, due to the other prominent spectral features in the surroundings.

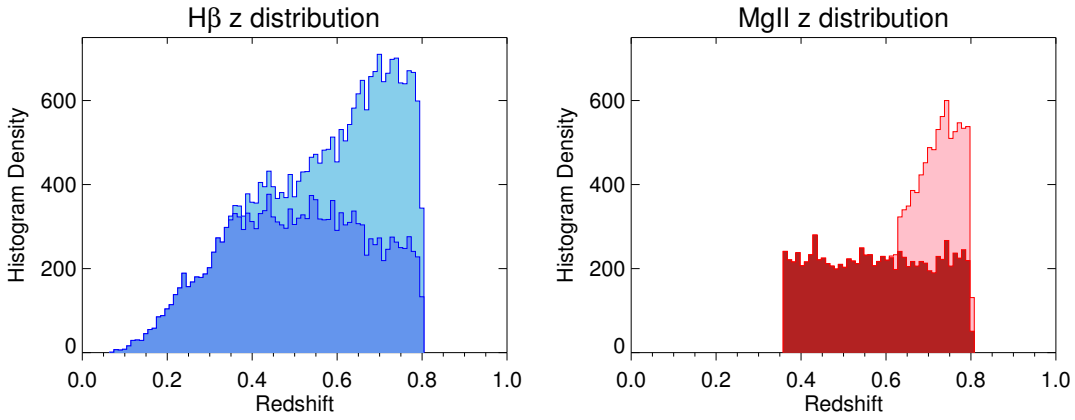

Figure 3.5 Redshift distribution of the QSO in our sample. Each broad emission line corresponds to a different selection of AGN in SDSS database, therefore *left* and *right* panel do not necessarily represent the same objects. *Azure* and *pink* histograms correspond to the cumulative DR10 database (also including DR7 sources); *blue* and *red* histograms represent only the old DR7 data.

In Figures from 3.8 to 3.14 we show some exempla of spectral fitting. In particular, from 3.8 to 3.10 we show DR7 Hβ spectra with decreasing S/N ratio. Black line is the original spectrum, with its errorbars in green, while our fitting curve is drawn in red. Yellow regions

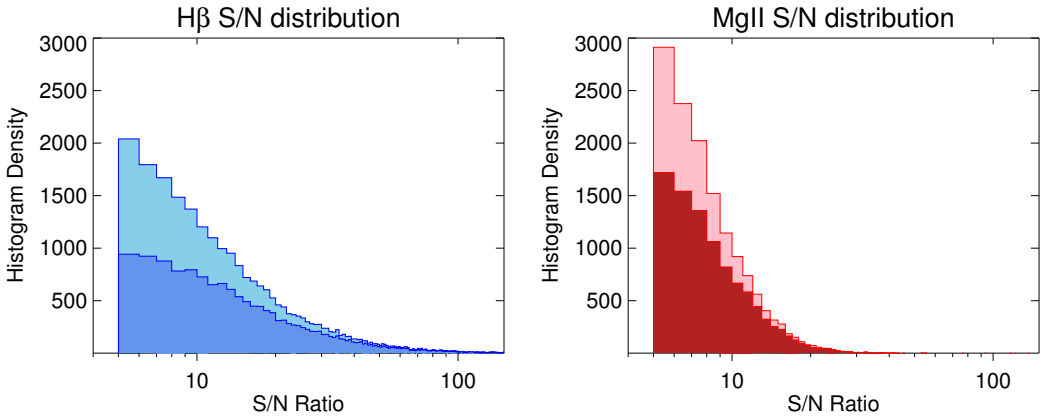

Figure 3.6 Signal to noise distribution of the QSO in our sample. Each broad emission line corresponds to a different selection of AGN in SDSS database, therefore *left* and *right* panel do not necessarily represent the same objects. *Azure* and *pink* histograms correspond to the cumulative DR10 database (also including DR7 sources); *blue* and *red* histograms represent only the old DR7 data.

represent the bad pixel we rule out from wavelength fitting range and from d.o.f. count. In each plot, the lower panel represent the residuals.

In Figure 3.14 we plot an example of a wrong fit, in which `IDL MPFIT` procedure does not converge. These sources are obviously ruled out in the following statistical interpretation of the data.

For an indicative comparison with the previous estimates by Shen et al. (2011) we also plot, in Figures 3.15 and 3.16 the results for $L(5100)$ and $L(3000)$. The plots compare the results for the DR7Q sources with a simultaneous estimate of the Hβ and the Mg II emission. From this sample, we show the estimates for a subset of objects with redshift $z \lesssim 0.8$, by imposing a S/N threshold of 5 and a χ^2/dof upper limit to 5. This selection corresponds to a 71% of the total number of sources with Hβ and Mg II detection. We notice a very strong correlation, with a Pearson correlation coefficient of $R = 0.973$ and a dispersion of less then 0.1 dex. An even better accordance is obtained when comparing the continuum luminosity in the Mg II wavelength range: the Pearson correlation parameter is $R = 0.994$ and the dispersion of the estimates is of less than 0.05 dex.

In Figures 3.17 and 3.18 we compare our Hβ and Mg II broad line widths estimates with

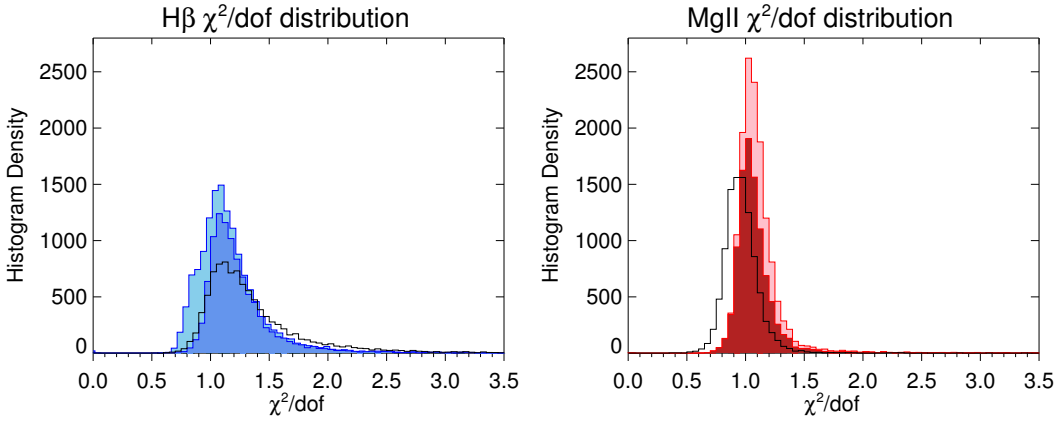

Figure 3.7 Reduced χ^2 distributions of the QSO in our sample computed by considering the whole broad line wavelength fitting range. Each broad emission line correspond to a different selection of AGN in SDSS database, therefore *left* and *right* panel do not necessarily represent the same objects. *Azure* and *pink* histograms correspond to the cumulative DR10 database (also including DR7 sources); *blue* and *red* histograms represent only the old DR7 data. In black the estimate for the same DR7 sources by Shen et al. (2011) (updated to their November 2013 results release).

previous results (same thresholds are applied). The FWHM appear to be only weakly correlated and the large observed dispersion illustrate the inferred line properties sensitivity to the adopted fitting procedure. In the case of the Hβ line the distribution is centered on the 1:1 relation , while, the distribution for the broad Mg II line is strongly asymmetric: our automatic fitting procedure finds almost systematic lower line widths with respect the estimates by Shen et al. (2011). For comparison we also plot in Figure 3.19 the histogram plots of the distributions of Hβ and Mg II broad line widths for the same sample of sources.

Finally, in Figures 3.20 and 3.21 we provide a comparison between the LL and VV diagrams. Our estimates for the continuum luminosities in the Hβ and Mg II wavelength ranges have a strong correlation and show a deviation from the 1:1 relation at high luminosities, in very good accordance with the results by Shen et al. (2011). The VV diagram show large discrepancy between our and Shen et al. (2011) results: our distribution appears to be shifted and tilted, consistently with the sharper distribution of Mg II FWHM shown in Figure 3.19.

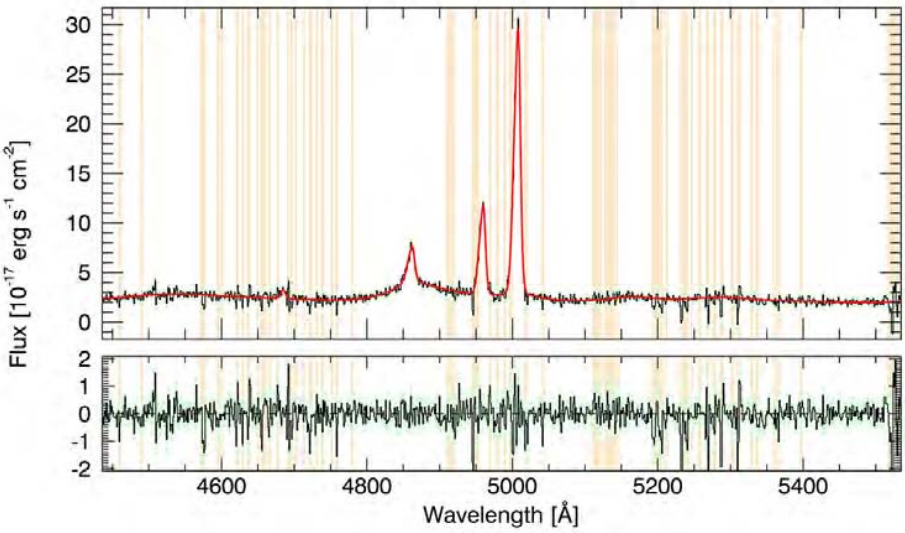

Figure 3.8 An example of a DR7 spectral fitting of the Hβ region. In *black* the original spectrum, fitted with the *red* curve. The Hβ broad line and the [O III] doublet are clearly visible. *Green* bars represent the flux uncertainty, while *yellow* stripes correspond to the avoided bad pixels. In the *lower panel* it is shown the residuals plot.

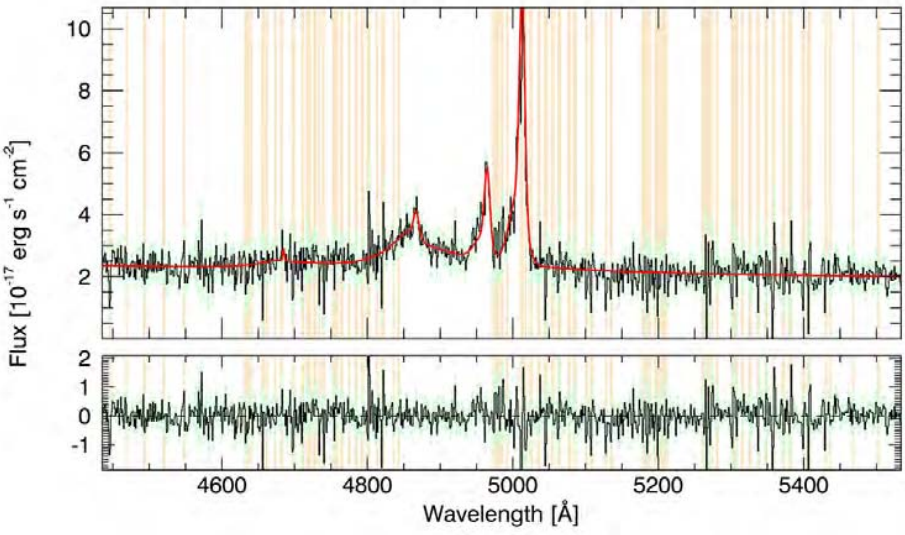

Figure 3.9 An example of a DR7 spectral fitting of the Hβ region. In *black* the original spectrum, fitted with the *red* curve. The Hβ broad line is clearly visible, while the [O III] doublet is very noisy. *Green* bars represent the flux uncertainty, while *yellow* stripes correspond to the avoided bad pixels. In the *lower panel* it is shown the residuals plot.

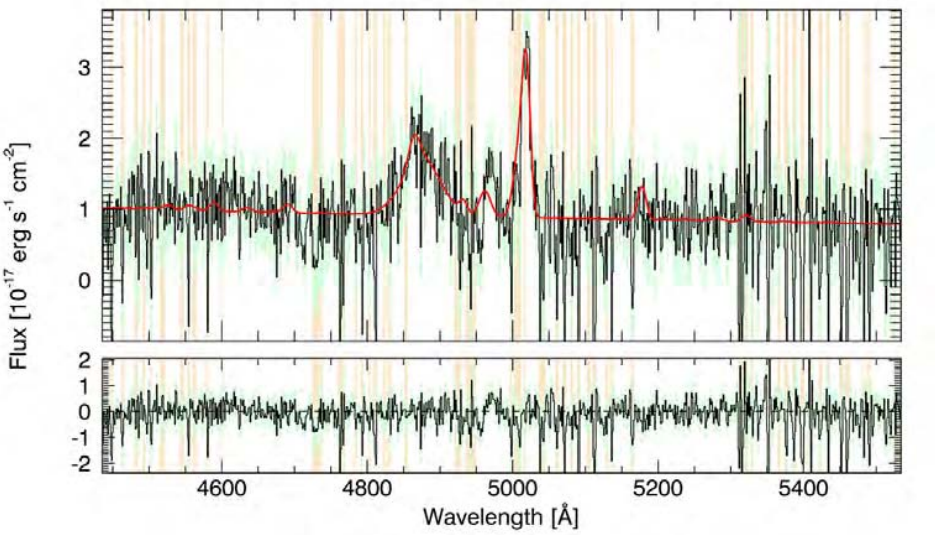

Figure 3.10 An example of a DR7 spectral fitting of the Hβ region. In *black* the original spectrum, fitted with the *red* curve. The Hβ broad line and the [O III] doublet are almost unrecognisable. *Green* bars represent the flux uncertainty, while *yellow* stripes correspond to the avoided bad pixels. In the *lower panel* it is shown the residuals plot.

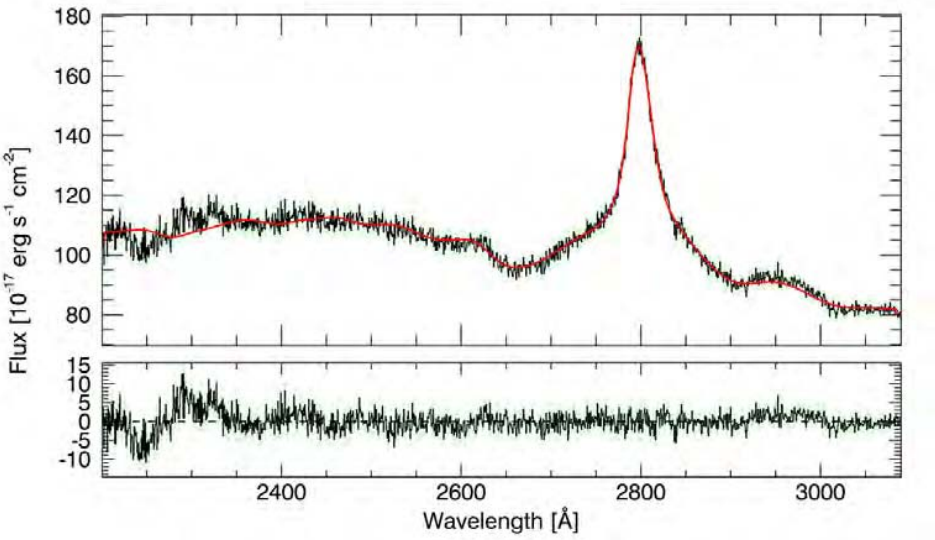

Figure 3.11 An example of a DR7 spectral fitting of the Mg II region. In *black* the original spectrum, fitted with the *red* curve. The Mg II broad line and the Fe II emission are clearly visible. *Green* bars represent the flux uncertainty. In the *lower panel* it is shown the residuals plot.

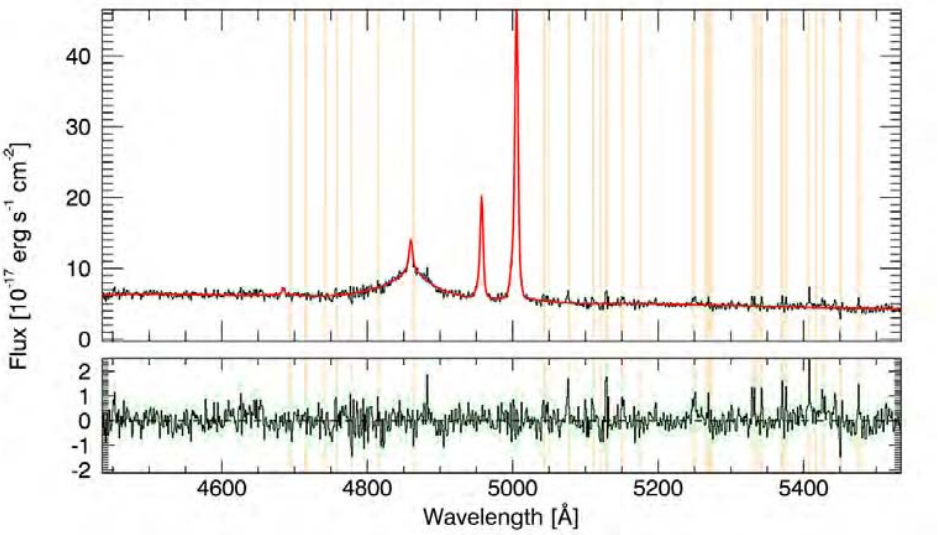

Figure 3.12 An example of a DR10 spectral fitting of the Hβ region. In *black* the original spectrum, fitted with the *red* curve. The Hβ broad line and the [O III] doublet are clearly visible. *Green* bars represent the flux uncertainty, while *yellow* stripes correspond to the avoided bad pixels. In the *lower panel* it is shown the residuals plot.

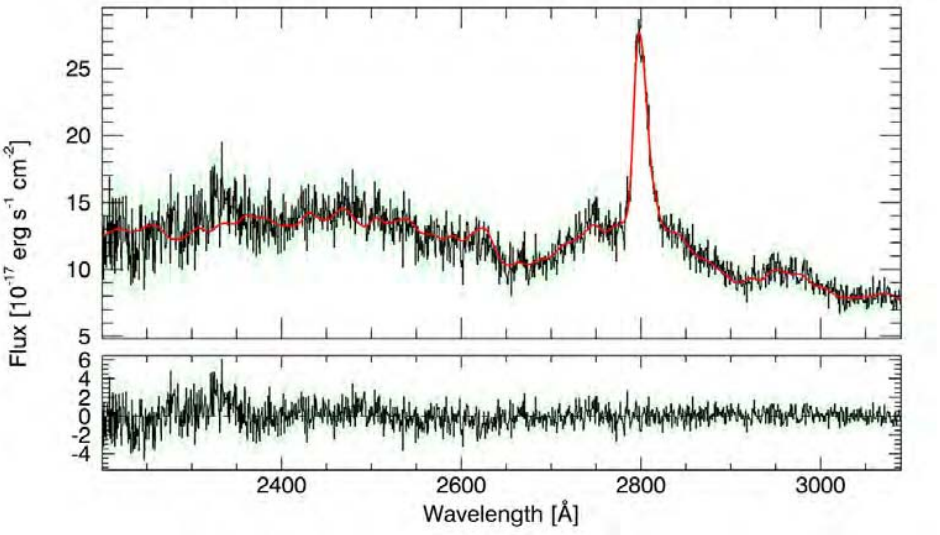

Figure 3.13 An example of a DR7 spectral fitting of the Mg II region. In *black* the original spectrum, fitted with the *red* curve. The Mg II broad line and the Fe II emission are clearly visible. *Green* bars represent the flux uncertainty. In the *lower panel* it is shown the residuals plot.

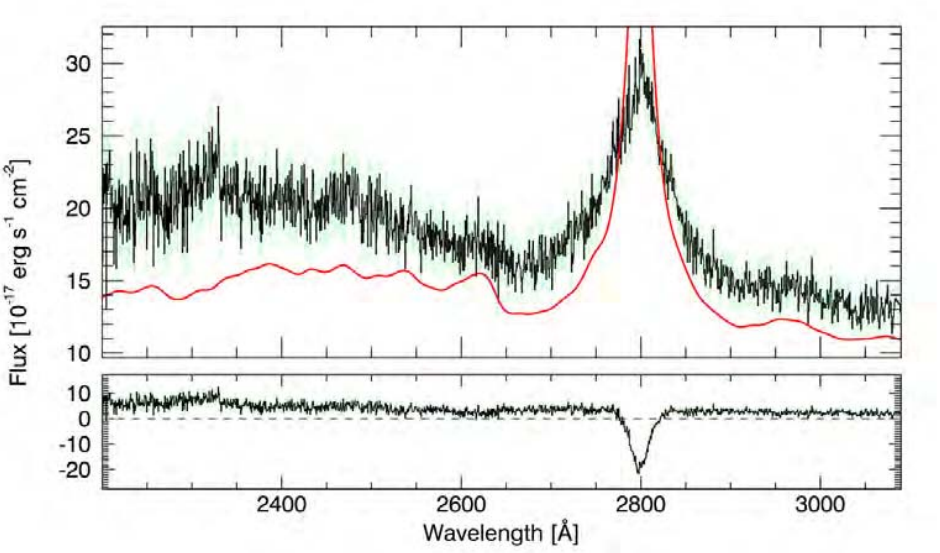

Figure 3.14 An example of a fitting failure. In this case the automatic procedures converges in a local minimum of the parameter space, not being able to reproduce the noisy Fe II emission and the Mg II broad line of a DR10 quasar.

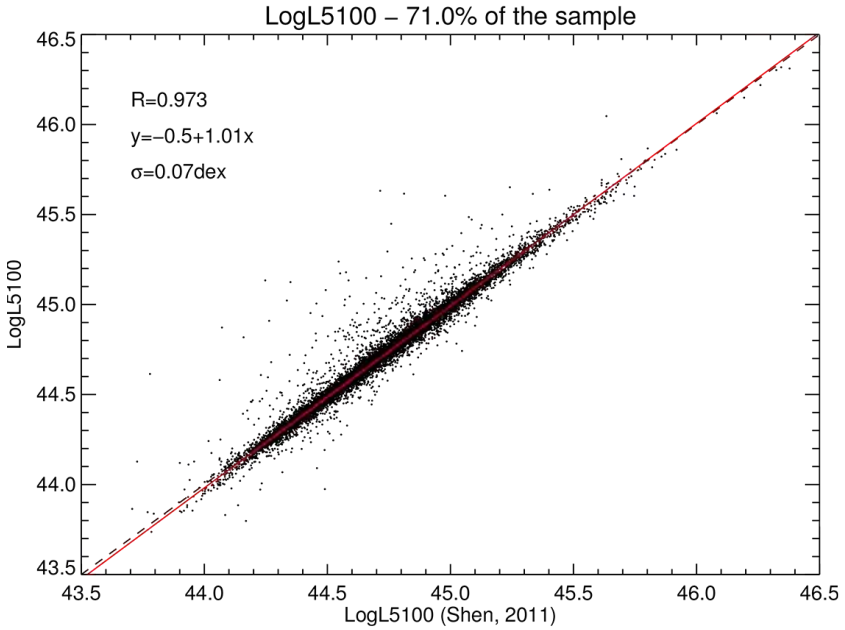

Figure 3.15 Comparison between our results for best fitting continuum luminosities at 5100Å and those by Shen et al. (2011) in the subset of sources with $z \lesssim 0.8$, S/N>5 and χ^2/dof<5. The Pearson correlation parameter R indicates a very strong correlation, with a very low dispersion σ. The *black* dashed line shows the 1:1 relation, while the solid *red* line shows the best linear relation obtained with a "robust" least absolute deviation method by using the `LADFIT` IDL routine.

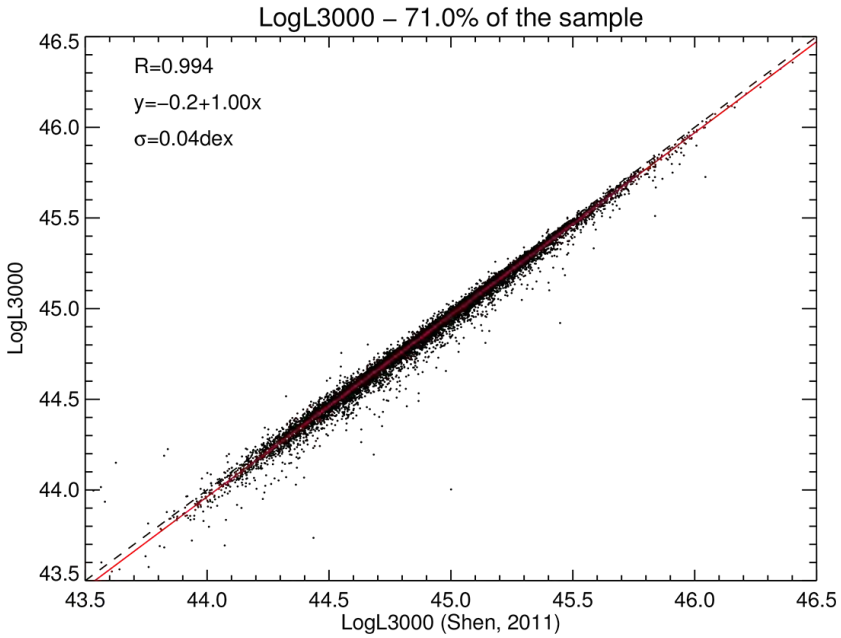

Figure 3.16 Comparison between our results for best fitting continuum luminosities at 3000Å and those by Shen et al. (2011) in the subset of sources with $z \lesssim 0.8$, S/N>5 and χ^2/dof<5. The Pearson correlation parameter R indicates a very strong correlation, with a very low dispersion σ. The *black* dashed line shows the 1:1 relation, while the solid *red* line shows the best linear relation obtained with a "robust" least absolute deviation method by using the `LADFIT` IDL routine.

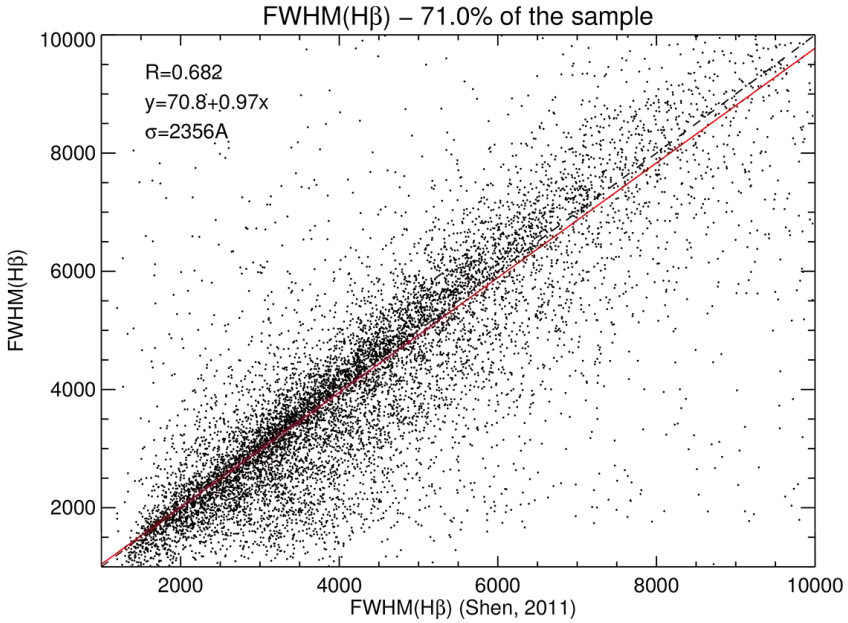

Figure 3.17 Comparison between our results for best fitting FWHM of the Hβ broad line and those by Shen et al. (2011) in the subset of sources with $z \lesssim 0.8$, S/N>5 and χ^2/dof<5. The Pearson correlation parameter R indicates a weak correlation between our and previous estimates, with a large dispersion σ. The distribution appears to be centered on the 1:1 relation, shown with a *black* dashed line. The solid *red* line shows the best linear relation obtained with a "robust" least absolute deviation method by using the `LADFIT` IDL routine.

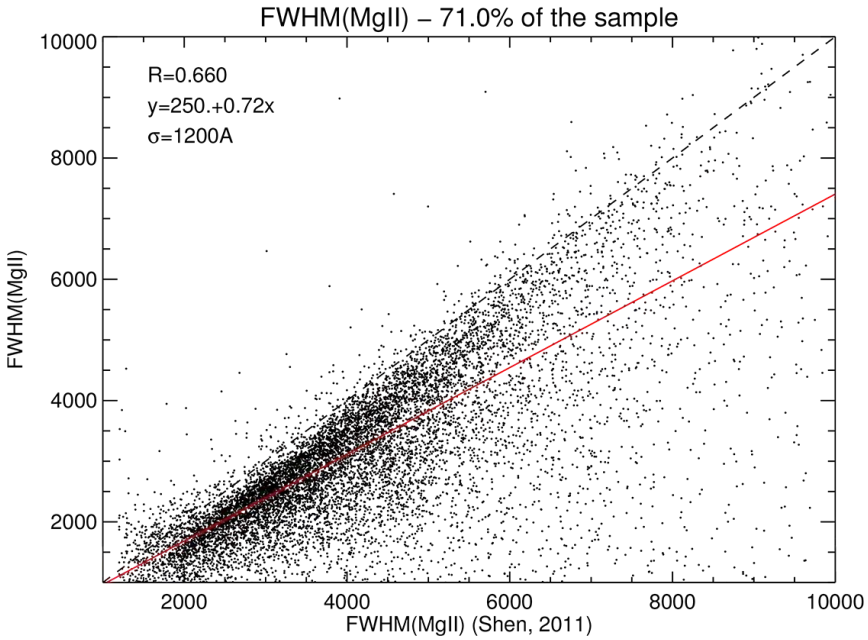

Figure 3.18 Comparison between our results for best fitting FWHM of the Mg II broad line and those by Shen et al. (2011) in the subset of sources with $z \lesssim 0.8$, S/N>5 and χ^2/dof<5. The Pearson correlation parameter R indicates a weak correlation between our and previous estimates, with a large dispersion σ. The distribution is not centered on the 1:1 relation, shown with a *black* dashed line. The solid *red* line shows the best linear relation obtained with a "robust" least absolute deviation method by using the `LADFIT` IDL routine.

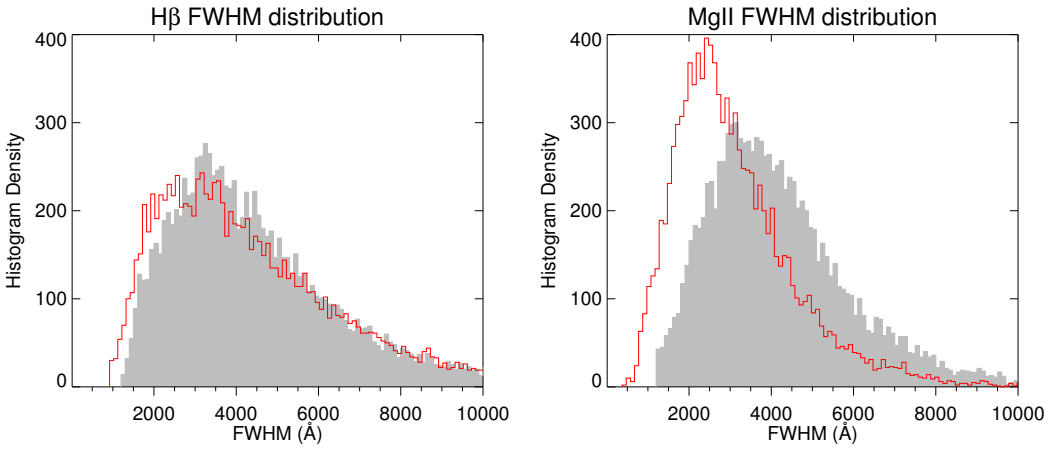

Figure 3.19 Comparison between our results for best fitting FWHM of the Hβ broad line and those by Shen et al. (2011) in the subset of sources with $z \lesssim 0.8$, S/N>5 and χ^2/dof<5. *Gray* filled histograms correspond to the estimate by Shen et al. (2011), while *red* histograms represent our results. The plots show similar distribution for the Hβ broad line widths, while in the case of Mg II we find an almost systematic shift towards lower values and a lower dispersion.

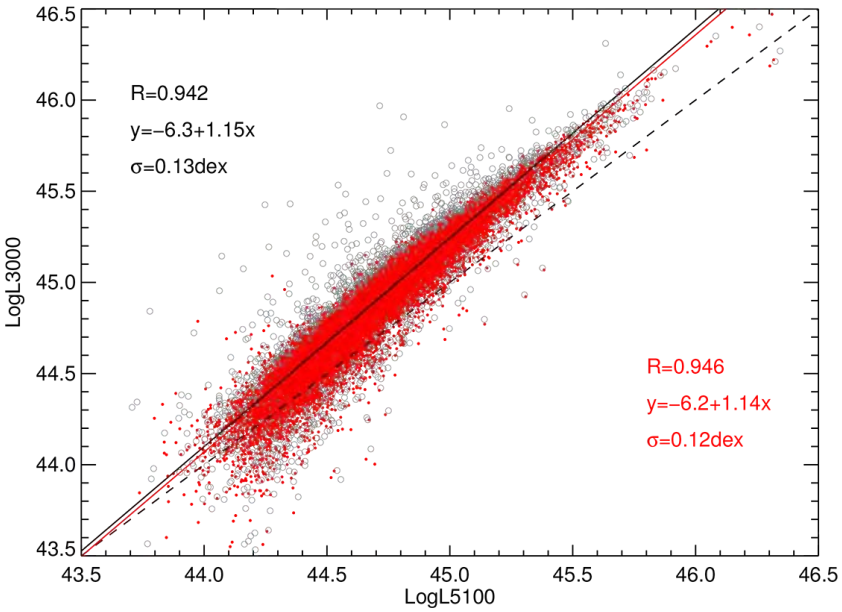

Figure 3.20 Comparison between our and Shen et al. (2011) results for the L(5100Å)-L(3000Å) continuum luminosity diagram. *Gray* empty circles show the results by Shen et al. (2011), while *red* points are our estimates. We only show a subset of sources with $z \lesssim 0.8$, S/N>5 and χ^2/dof<5. The Pearson correlation parameter R indicates very strong correlations, with very low dispersions σ. The *black* dashed line shows the 1:1 relation, while the solid *red* line shows the best linear relation obtained with a "robust" least absolute deviation method by using the `LADFIT` IDL routine.

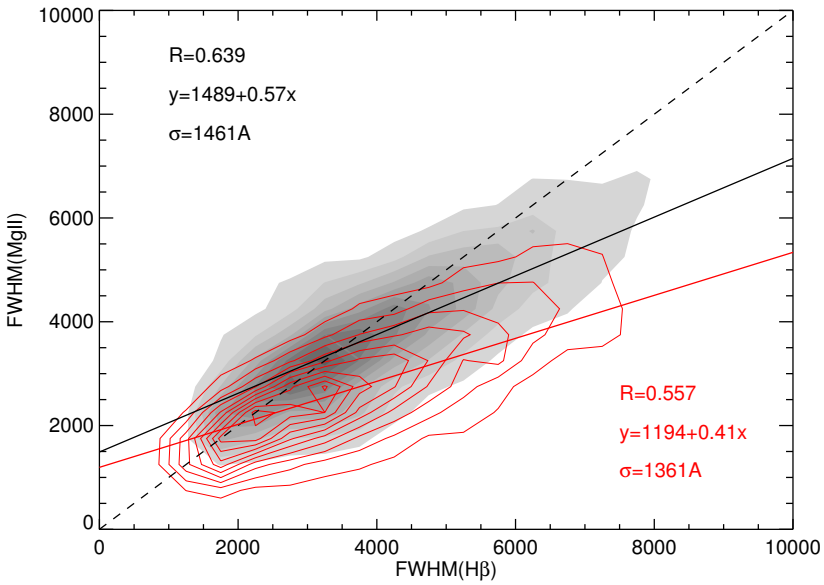

Figure 3.21 Comparison between our and Shen et al. (2011) results for the FWHM(Hβ)-FWHM(Mg II) diagram. *Gray* filled contour levels represent the probability densities by Shen et al. (2011), while the *red* superimposed levels are our corresponding estimations. Our distribution is shifted and tilted with respect to the one by Shen et al. (2011), while the dispersions are similar.

Chapter 4

The effect of radiation pressure on virial black hole masses based on Hβ, Mg II and C IV broad emission lines

4.1 Introduction

In the last few years, it has become increasingly clear that supermassive black holes (BH) are an essential element in the evolution of galaxies. The key observational evidence of a link between a BH and its host galaxy is provided by the tight correlations between BH mass and luminosity, mass, velocity dispersion and surface brightness profile of the host spheroids (Kormendy & Richstone 1995; Gebhardt et al. 2000a; Ferrarese & Merritt 2000; Marconi & Hunt 2003; Graham et al. 2007; Graham 2008; Gültekin et al. 2009; Hu 2009; Kormendy & Bender 2009; Sani et al. 2011). The link between BH and host galaxy is probably established by the feedback of the accreting BH, i.e. the active galactic nucleus, on the host galaxy itself (e.g. Silk & Rees 1998; Granato et al. 2004; Di Matteo et al. 2005; Croton et al. 2006; Menci et al. 2008; Marulli et al. 2008; Hopkins et al. 2009; Cattaneo et al. 2009; Ciotti et al. 2009, and references therein).

In order to fully understand the implications of BH growth on the evolution of the host galaxies it is fundamental to measure BH masses in large samples of galaxies from zero to

high redshifts. Direct BH mass estimates based on stellar and gas kinematics are possible only in the local universe and their complexity does not allow their application to large samples (e.g. Ferrarese & Ford 2005; Marconi et al. 2006). The limit of the local universe can be overcome by considering a BH "mass ladder" similar to the extragalactic distance scale (Peterson, 2004).

Rung one of the BH mass ladder is provided by spatially resolved gas and stellar kinematical mass measurements in the local universe resulting in the $M_{\rm BH}$-$\sigma_{\rm e}$ and $M_{\rm BH}$-$L_{\rm sph}$ scaling relations.

Rung two is provided by virial BH masses estimated with the reverberation mapping (RM) technique; BH masses are given by $M_{\rm BH} = f\Delta V^2 R_{\rm BLR}/G$, where $R_{\rm BLR}$ is the Broad Line Region (BLR) average distance from the BH estimated with reverberation mapping, ΔV is the width of the broad emission line from average or rms spectra and f is a scaling factor which depends on the physical properties of the BLR (e.g. Peterson & Wandel 2000). Although this technique is potentially plagued by many unknown systematic errors (Krolik, 2001), BH masses from reverberation mapping are in agreement with the $M_{\rm BH}$-$\sigma_{\rm e}$ relation of normal galaxies (e.g. McLure & Dunlop 2002; Onken et al. 2004; Greene & Ho 2006). The calibration of the second rung has been performed by Onken et al. (2004) who have provided an estimate of f assuming that the AGN with RM observations follow the $M_{\rm BH}$-$\sigma_{\rm e}$ relation of normal galaxies (Tremaine et al., 2002; Ferrarese & Ford, 2005).

In principle rung two allows $M_{\rm BH}$ measurements without any distance limits but RM observations needed to estimate $R_{\rm BLR}$ in high-z AGN are exceedingly demanding in term of telescope time (e.g. Kaspi et al. 2007). The radius-luminosity relation discovered by Kaspi et al. (2000) indicates that continuum luminosity can be used as a proxy for $R_{\rm BLR}$ (see also Kaspi et al. 2005; Bentz et al. 2006b; Bentz et al. 2009) leading to single epoch (SE) virial BH mass estimates and rung three in the BH mass ladder. The physical origin of the radius-luminosity relation has been discussed in Chapter 2, where we have found that size estimates from Hβ and MgII should have similar accuracy but those from CIV might be potentially worse.

The calibration of step three has been performed by many authors (Laor 1998; McLure &

Dunlop 2002; McLure & Jarvis 2002; Vestergaard 2002; Wu et al. 2004; Greene & Ho 2005; Vestergaard & Peterson 2006; McGill et al. 2008). In particular, Vestergaard & Peterson (2006) considered $M_{\rm BH}$ from reverberation mapping to calibrate SE virial estimates for the same objects. SE BH masses are deemed accurate only from a statistical point of view on large samples of objects since a single measurement can be wrong even by a factor of ~ 10 (e.g. Vestergaard & Peterson 2006). A thorough analysis of the systematic uncertainties affecting SE mass estimates is presented by Denney et al. (2009). Many groups are routinely using them to estimate BH masses in large sample of galaxies from zero to high redshifts (e.g. Willott et al. 2003; McLure & Dunlop 2004; Treu et al. 2004; Vestergaard 2004; Jiang et al. 2007; Netzer et al. 2007; Salviander et al. 2007; Shen et al. 2009; Woo et al. 2008; Merloni 2009; Greene & Ho 2009).

Marconi et al. (2008) considered the effect of radiation pressure from ionizing photons on RM and SE virial black hole masses based on the broad Hβ emission line. They showed that BH masses based only on the virial product $\Delta V^2 R$ and neglecting the effect of radiation pressure can be severely underestimated especially in objects close to the Eddington limit. They then provided an empirical calibration of the correction for radiation pressure and showed that it is consistent with a simple physical model in which BLR clouds are optically thick to ionizing radiation and have average column densities of $N_{\rm H} \sim 10^{23}\,{\rm cm}^{-2}$. This value is remarkably similar to what is used in standard BLR photoionization models to explain observed spectra (see, e.g., Chapter 2). With the inclusion of radiation pressure the discrepancy between RM (rung two) and SE (rung three) virial BH masses drops from 0.4 to 0.2 dex rms. The use of single epoch observations as surrogates of reverberation mapping campaigns can thus provide more accurate BH masses than previously thought. Marconi et al. (2008) also showed that Narrow Line Seyfert 1 (NLS1) galaxies have apparently low BH masses because they are radiating close to their Eddington limit. After the radiation pressure correction, NLS1 galaxies have BH masses similar to other broad line AGN and follow the same $M_{\rm BH}$-$\sigma_{\rm e}/L_{\rm sph}$ relations as other active and normal galaxies. These results led them to the conclusion that radiation forces arising from ionizing photon momentum deposition constitute an important physical effect which must be taken into account when computing

virial BH masses.

4.2 Overview of the radiation pressure correction and of tests on its importance

The zero order correction for radiation pressure is simply proportional to the continuum luminosity, therefore the virial BH mass can be expressed as

$$M_{\rm BH} = f V^2 L_c^{\alpha} + g L_c \tag{4.1}$$

where V the width of a broad emission line, L_c is the luminosity (λL_λ) of the adjacent continuum and α is the slope of the radius-luminosity relation for the BLR. The scaling factors f and g can be empirically calibrated as described by Marconi et al. (2008). The physical meaning of the empirically calibrated g value can be found using a simple model in which radiation pressure is dominated by the absorption of ionizing photons by optically thick BLR clouds which re-emit isotropically reprocessed radiation. In this model the correction for radiation pressure is (Marconi et al., 2008):

$$\begin{aligned} g L_c &= \frac{b_{ion} b_c}{4\pi G \mu m_{\rm p} c N_{\rm H}} L_c = 5.0 \times 10^7 \, {\rm M}_\odot \times \\ &\times \left(\frac{L_c}{10^{44} \, {\rm erg \, s^{-1}}} \right) \left(\frac{b_{ion} \times b_c}{0.5 \times 10.0} \right) \left(\frac{\mu}{1.2} \right)^{-1} \left(\frac{N_{\rm H}}{10^{23} \, {\rm cm^{-2}}} \right)^{-1} \end{aligned} \tag{4.2}$$

where b_{ion} and b_c are the correcting factors which transform ionizing luminosity and L_c into bolometric luminosity, μ is the average molecular weight in units of m_p the proton mass and $N_{\rm H}$ is the average column density of BLR clouds in the direction of the ionizing radiation source.

More refined forms of the correction for radiation pressure can take into account, e.g., a luminosity dependence of the bolometric corrections (e.g. Marconi et al. 2004) or of the average cloud column density, although such refinements are likely excessive compared to the level of accuracy of the virial term.

The core of the problem is not the existence of a radiation pressure correction or of its analytical form: as far as BLR clouds are photoionized, an outward radiative force due to the absorption of ionizing photons must exist. The main open issue is the magnitude of the radiation pressure correction and, in particular, the column density of BLR clouds: if most BLR clouds have large column densities (e.g. $N_{\rm H} > 10^{24}\,{\rm cm}^{-2}$), then radiation forces are negligible compared to gravitational ones. So far two papers have tried to address this issue (Netzer, 2009; Onken, 2009).

Netzer (2009) proposed a test on the importance of radiation pressure which is based on the comparison between the observed distributions of $M_{\rm BH}$ and $L/L_{\rm Edd}$ in two samples of type 1 and 2 AGN respectively, which were supposedly drawn from the same parent distribution, assuming that type 1 and type 2 AGN have the same L/L_{Edd} distribution. In the sample of type 2 AGN, BH masses were estimated from stellar velocity dispersions of the host galaxy and the $M_{\rm BH}-\sigma$ relation, supposedly providing the correct BH mass values. In the sample of type 1 AGN, BH masses were estimated with the virial theorem, with and without the radiation pressure correction. Netzer (2009) noted that, with the radiation pressure correction, the $L/L_{\rm Edd}$ distribution is truncated at ~ 0.15 and inconsistent with that derived from the type 2 AGN sample, which is however well in agreement with that based on virial masses without radiation pressure correction.Netzer (2009) then concluded that BLR clouds should have large column densities ($N_{\rm H} \sim 10^{24}\,{\rm cm}^{-2}$) in order not to be affected by radiation pressure.

Marconi et al. (2009) then showed that Netzer (2009) conclusions are not unique. In general, the comparison between the $L/L_{\rm Edd}$ distributions can only show that there should exist a distribution of $N_{\rm H}$ values in BLRs, and that only a small fraction of all AGN should have large average column densities. In any case, the comparison proposed by Netzer (2009) is physically sound and does allow us to conclude that one must take into account a possible distribution of $N_{\rm H}$ values. Indeed, a distribution of $N_{\rm H}$ values for BLR clouds is also suggested by the analysis of broad Fe II emission (Ferland et al., 2009) but, most importantly, such distribution is found in the few cases where direct $N_{\rm H}$ measurements for BLR clouds are possible (Risaliti et al. 2007, 2009b,a; Risaliti 2009).

Onken (2009) proposed a new test on the importance of radiation pressure. He suggested

that one should observe a variation of the virial product with continuum luminosity. Indeed, the virial product provides information of the shielded gravitational field as seen by BLR clouds, i.e.

$$\mathrm{VP} = f\frac{V^2 R_{\mathrm{BLR}}}{G} = M_{\mathrm{BH}} - g\,L_c \tag{4.3}$$

therefore the virial product should vary linearly with continuum luminosity. Onken (2009) tested this statement with NGC5548 data and did not found the expected VP variations with luminosity, on the contrary the virial product appeared to increase with increasing luminosity. However, the argument by Onken (2009) does not take into account that BLR dynamics is not affected by the instantaneous luminosity of the AGN but by its average value over the past dynamical timescale. Thus, the argument by Onken has no validity since it uses instantaneous luminosities which only affect the ionization structure of the BLR, not its dynamical state. The typical dynamical timescale can be simply estimated with the orbital period of a circularly rotating BLR cloud

$$\tau_{dyn} = \frac{2\pi R_{\mathrm{BLR}}}{V_{\mathrm{BLR}}} \simeq 14\,\mathrm{yr}\left(\frac{R_{\mathrm{BLR}}}{8\ \mathrm{light-days}}\right)^{1.5} \tag{4.4}$$

where we have used the best fit relation between the velocity dispersion of the broad line in the rms spectrum (σ) and the time lag for Hβ from the multi epoch observations of NGC 5548 (Bentz et al., 2007)

$$V_{\mathrm{BLR}} = \sigma \simeq 3000\,\mathrm{km\,s}\left(\frac{R_{\mathrm{BLR}}}{8\ \mathrm{light-days}}\right)^{-0.5} \tag{4.5}$$

Clearly, the dynamical time-scale of NGC 5548 BLR clouds is much longer than the timescale of luminosity variations which have been used by Onken (2009) to claim that radiation pressure is not important. In conclusions, the argument by Onken (2009) that radiation pressure is not important is not valid because it neglects that the dynamical structure of the BLR can only change on a dynamical timescale.

4.3 Possible Observational Evidences for Radiation Pressure

To assess the importance of the radiation forces on BLR clouds dynamics, we will now identify some observational results which can be coherently explained when considering the effect of radiation pressure.

The first observational result is obtained from the analysis of Netzer (2009) and Marconi et al. (2009) presented in the previous section which suggests that BLR clouds have very likely a distribution of column density values such that they will be affected by radiation forces to different extents. In particular, lines which are predominantly emitted from high $N_{\rm H}$ clouds (e.g. Mg II, see also Chapter 2 where we discuss the physical origin of the R-L relation) will be less affected by radiation pressure than others (e.g. Hβ and C IV). Apart from being more realistic, the existence of a distribution of $N_{\rm H}$ values is also suggested by the analysis of redshifted broad Fe II emission in quasar spectra performed by Ferland et al. (2009), and most importantly, by the only existing direct measurements (Risaliti, 2009, and references therein)

The second observational result is the non-linearity between line widths of different broad emission lines or between FWHM and σ's of the same emission lines which is observed in various AGN samples. Wang et al. (2009) investigated the relationship between the line widths of broad Mg II and Hβ lines, providing refined virial BH mass estimators. In more details they start from noticing that the line widths (FWHM) of Mg II and Hβ from single epoch spectra are not following a linear relation, suggesting that the two lines are not co-spatial. Furthermore, they find that the velocity dispersion σ of the Hβ line from *rms* spectra has not a linear relation with neither $FWHM(\mathrm{Mg\,II}, SE)$ (i.e. from single epoch spectra) nor $FWHM(\mathrm{H}\beta, mean)$ (i.e. from *mean* spectra from RM campaigns). Such behavior had already been noticed by Collin et al. (2006) who provided empirical correction to better recover from FWHM(Hβ, SE) an estimate of $\sigma(\mathrm{H}\beta, rms)$ believed to be the best indicator of the virial velocity (Peterson et al., 2004). Wang et al. (2009) interpreted phenomenologically these non linearities as an indication that in single epoch virial estimates the velocity term

should be allowed an exponent different from 2. Indeed, their newly calibrated virial mass estimators for Hβ and Mg II provide an improvement over previous work, which does not take into account radiation pressure. From the results by Wang et al. (2009) we identify two distinct non-linear relations which are caused by different physical reasons:

- the non-linear relation between $FWMH$ and σ of broad Hβ in *rms* spectra obtained during RM campaigns;
- the non-linear relation between the $FWMH$ of broad Hβ and the $FWHM$ of broad Mg II from the same single-epoch spectra.

The non-linear relations identified by Wang et al. (2009) are just one of the two or a combinations of both.

The third result is the variation of broad line profile shapes with line width and $L/L_{\rm Edd}$. In a series of papers, J. Sulentic, P. Marziani and collaborators have proposed the existence of 2 populations of broad line AGN whose properties vary between 'Population A' ($FWHM < 4000\,{\rm km\,s}$) and 'Population B' ($FWHM > 4000\,{\rm km\,s}$) sources (e.g. Sulentic et al. 2006; Marziani et al. 2008; Sulentic et al. 2008, 2007; Marziani et al. 2009 and references therein). In particular, 'Population A' sources are characterized by "spiky" line profiles, best described by Lorentzian functions while 'Population B' sources have "bell-shaped" line profiles best described by (multiple) Gaussian functions. Incidentally spiky line profiles are characteristic of high luminosity quasars (Nagao et al., 2006). In this A-B classification, Narrow Line Seyfert 1 galaxies belong to Population A and do not emerge as a distinct class (Sulentic et al., 2007). Finally, the empirical separation between population A and B set to $FWHM \approx 4000\,{\rm km\,s}$, appears to be related to a critical value of the Eddington ratio ($\approx 0.2 \pm 0.1$, Marziani et al. 2009).

In this thesis we will provide a coherent physical interpretation of these observational results. At first, we will first calibrate virial BH masses based on Hβ Mg II and C IV taking into account the correction for radiation pressure or the simple virial relation adopted so far. We will then use these calibrations to explain the above facts with the effect of radiation pressure on BLR clouds.

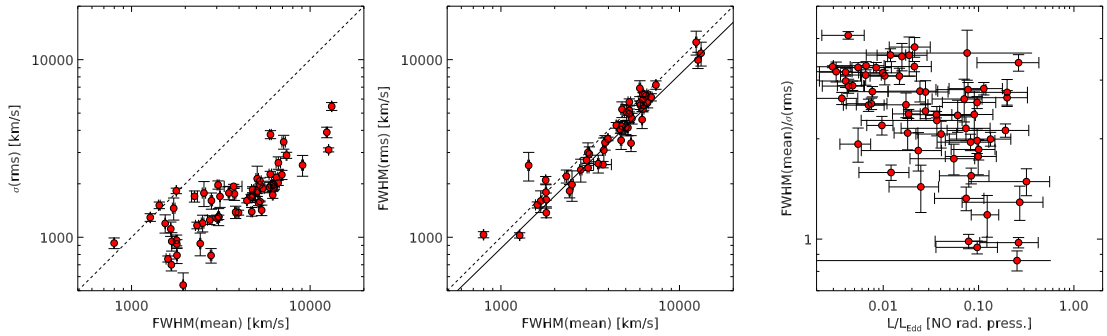

Figure 4.1 Left: relation between Hβ velocity dispersion from rms spectra and FWHM of mean spectra. Center: relation from Hβ FWHM in rms and mean spectra. Right: ratio between Hβ FWHM from mean spectra and velocity dispersion from rms spectra plotted as a function of L/L_{Edd}. The dotted lines denote the 1:1 relation, while the solid one in the central panel is the linear fit to the observed data.

4.4 Calibration of $M_{\rm BH}$ based on Hβ

We start by calibrating virial BH masses from RM data by comparing virial products with BH mass estimates from $M_{\rm BH}-L,\sigma$ correlations, $M_{\rm BH}(\sigma,L)$. This is the same approach followed by Onken et al. (2004). We then calibrate virial BH masses for SE spectra. At variance with Vestergaard & Peterson (2006) and Marconi et al. (2008) we will not calibrate $M_{\rm BH}$(SE) to $M_{\rm BH}$(RM) but directly to $M_{\rm BH}(\sigma,L)$, since all the galaxies in the RM database have now either a σ or L measurement for the bulge. This approach is clearly more direct than the two-steps one followed in previous papers.

We consider the database of line widths measurements collected by Peterson et al. (2004), in the form presented by Collin et al. (2006) in their table 1 which provides time lags (τ_{cen} from cross correlation centroids), $FWHM$ and σ for both *mean* and *rms* spectra obtained during all RM campaigns performed so far. Since some objects have several independent measurements, we used all of them. We update this database by including the more recent data by Bentz et al. (2006a); Denney et al. (2006); Bentz et al. (2007); Grier et al. (2008); Bentz et al. (2009); Denney et al. (2010); Grier et al. (2012); Dietrich et al. (2012); Park et al. (2012).The average continuum luminosities are obtained by Bentz et al. (2009) who correct for the host galaxy emission.

We consider bulge V-band luminosities from Bentz et al. (2009) and velocity dispersions

from Nelson et al. (2004), Onken et al. (2004), Dasyra et al. (2007), Watson et al. (2008), Woo et al. (2010), Barth et al. (2011), Grier et al. (2013). To estimate BH masses we use the $M_{\rm BH}-L_V$ and $M_{\rm BH}-\sigma$ relations estimated by Gültekin et al. (2009). When an object has both σ and L_V we take the error-weighted logarithmic-mean of the corresponding BH masses.

In figure 4.1 we compare the $FWHM$ of the broad Hβ line from *mean* spectra with the σ (left) and $FWHM$ (center) from *rms* spectra. At variance with Wang et al. (2009), we plot the datapoints from the single RM campaigns and not the object-based averages. It is clear from the left panel that the $FWHM$ of the *mean* spectra and the σ of the *rms* spectra are not linear, while the $FWHM$ of *mean* and *rms* do follow a linear relation, although the former are 20% larger on average. This non-linear relation has also been noted by Wang et al. (2009).

In the right panel of figure 4.1 we compare the ratio $FWHM(mean)/\sigma(rms)$ with the $L/L_{\rm Edd}$ ratio, computed with the classical virial relation, i.e. without taking into account the correction for radiation pressure (e.g., as in eq. 4.6 below without the second term). Albeit with a large scatter there is a clear anti-correlation between $FWHM(mean)/\sigma(rms)$ and $L/L_{\rm Edd}$. At increasing $L/L_{\rm Edd}$, $\sigma(rms)$ increases for a given $FWHM(mean)$. This result just represents the sequence from Pop. A to B sources found by Marziani et al. (2009). Since $FWHM(rms)$ vs $FWHM(mean)$ is linear, the non linear $\sigma(rms)$ vs $FWHM(mean)$ relation is not due to the choice of *rms* spectra instead of *mean* ones but is the result of the change in line profile shape which is encountered along the Pop. A - Pop. B sequence.

We now follow Onken et al. (2004) and calibrate virial BH masses using the virial product estimated from RM data. We estimate virial products using the above database, discarding data from Mrk79 (1 data point out of 4), PG9844+349, NGC3227 (2 data points out of 3), NGC3516 (1 out of 2), NGC40541 (1 out of 2), NGC4151 (1 out of 2), PG1211+143, NGC4593 (1 out of 2), IC4329A, PG2130+099 (2 out of 3), because their RM data are not reliable (Peterson et al., 2004).

As in Marconi et al. (2008), we write the virial BH mass estimates as

$$M_{\rm BH} = 10^f \frac{V^2 R_{\rm BLR}}{G} + 10^g \left(\frac{L_{5100}}{10^{44}\,{\rm erg\,s^{-1}}}\right) {\rm M}_\odot \tag{4.6}$$

where V is the $\sigma(rms)$ of the broad Hβ line, $R = c\tau_{cen}$ where τ_{cen} is the time-lag of Hβ estimate from the centroid of the cross-correlation peak (Peterson et al., 2004) and L_{5100} represents λL_λ at 5100Å.

f and g are then derived by finding the minimum of:

$$\chi^2 = \sum_i \frac{[(\log M_{\rm BH})_i - (\log M_{\rm BH})_{0,i}]^2}{(\delta \log M_{\rm BH})_i^2 + (\delta \log M_{\rm BH})_{0,i}^2 + \Delta\Sigma^2} \tag{4.7}$$

where $(\log M_{\rm BH})_i$ is the log BH mass of the i-th object which depends on f and g, $(\log M_{\rm BH})_{0,i}$ is the expected mass value from the $M_{\rm BH} - \sigma, L$ relations described above, $(\delta \log M_{\rm BH})_i$, is the error on $(\log M_{\rm BH})_i$ based on the errors on V^2, R and $(\delta \log M_{\rm BH})_{0,i}$ is the error on $(\log M_{\rm BH})_{0,i}$ based on the errors on σ, L. At variance with Onken et al. (2004), we allow for an intrinsic dispersion of the $M_{\rm BH} - \sigma, L$ relations, $\Delta\Sigma$, which we take equal to 0.4 dex (Gültekin et al., 2009). We follow a standard χ^2 minimization and estimate errors on the parameters with the bootstrap method (Efron & Tibshirani, 1994) with 1000 realizations of the parent sample.

Results are shown in Fig. 4.2 and Tab. 4.1. Top and bottom panels in figure represent the cases without and with radiation pressure, respectively. Central and right panels compare $M_{\rm BH}(RM)$ vs $M_{\rm BH}(\sigma, L)$ (center) and their ratio vs $M_{\rm BH}(\sigma, L)$. The top left panel presents the χ^2 value for the variation of f in the case of no radiation pressure; the dashed horizontal lines represent the minimum χ^2 and 1σ values. In the lower left panel, the image represents the χ^2 value for the joint variation of f and g, the circle the minimum χ^2 value while the contours represent $\Delta\chi^2_{min} + [2.30, 4.61, 9.21]$, i.e. the 68%, 90%, 99% confidence contours for two significant parameters (Avni 1976).

From table and figure, it is clear that including the correction for the radiation pressure does not improve the accuracy of $M_{\rm BH}(RM)$ compared to the masses expected from the $M_{\rm BH} - \sigma, L$ correlations. In both cases the intrinsic dispersion of the residuals, $\log M_{\rm BH}(RM)/M_{\rm BH}(\sigma, L)$, is ~ 0.4 dex. Moreover, the data only allow to place an upper limit to g. To check for possible systematic errors due to the fact that the number of RM mapping measurements is not the same for all objects, we have also considered one data point per object given by the weighted average of the existing measurements.

As we have discussed previously, the line velocity dispersion might not trace the virial (rotational) velocity if there are broad wings due to fast outflowing material, expected when the radiation pressure is important. Therefore, we also calibrate virial masses using $FWHM(mean)$ for V. Results are shown in Fig. 4.3 and Tab. 4.1.

Without radiation pressure, the use of $FWHM(mean)$ or $\sigma(rms)$ provide similar accuracies of $M_{\rm BH}(RM)$ (0.41 dex and 0.42 dex dispersion, respectively). However, using $FWHM(mean)$, there is a significant improvement with the inclusion of the radiation pressure correction: the intrinsic dispersion drops from 0.43 to 0.31 dex and the improvement is also clear when comparing the left panels of Fig. 4.3. Using $FWHM(mean)$ and considering the correction for radiation pressure one can get $M_{\rm BH}(RM)$ estimates which have a comparable accuracy to those obtained using $\sigma(rms)$. In practice, $FWHM(mean)$ can be measured from spectra with a much larger S/N and is not affected by broad, faint wings. The fact that $M_{\rm BH}(RM)$ estimates with $\sigma(rms)$ and no radiation pressure correction are equivalent to those with $FWHM(mean)$ and the radiation pressure correction has the simple physical explanation that $\sigma(rms)$ is affected by broad wings of non virialized (possibly outflowing) material. These wings are stronger when radiation pressure is stronger increasing $\sigma(rms)$ and providing a similar increase on $M_{\rm BH}(RM)$ to that of the radiation pressure correction.

In conclusion, the virial BH mass estimator from reverberation mapping data can be obtained from eq. 4.6 using $V = FWHM(mean)$, $R = c\tau_{cen}$ and $f = -0.12\,(+0.19, -0.24)$, $g = 7.73\,(+0.26, -0.35)$.

We will now calibrate SE virial masses. At variance with Vestergaard & Peterson (2006) and Marconi et al. (2008) we do not rely on the calibration for $M_{\rm BH}(RM)$ but we directly calibrate $M_{\rm BH}(SE)$ from $M_{\rm BH}(\sigma, L)$: all sources in the RM database have now an estimate of $M_{\rm BH}$ from bulge properties (Bentz et al. 2009) and the calibration from $M_{\rm BH}(\sigma, L)$ is more direct. To calibrate SE masses we use the same data used previously and $V = FWHM(mean)$, since $FWHM(mean)$ is more directly related to a single epoch FWHM measurement. Since in SE spectra there are no information on the BLR time lag, we use the radius-luminosity correlation (Kaspi et al., 2000, 2005; Bentz et al., 2006b; Bentz et al., 2009) which, in its most recent determination, is simply $R \propto L^{0.5}$. Therefore, we calibrate the following virial

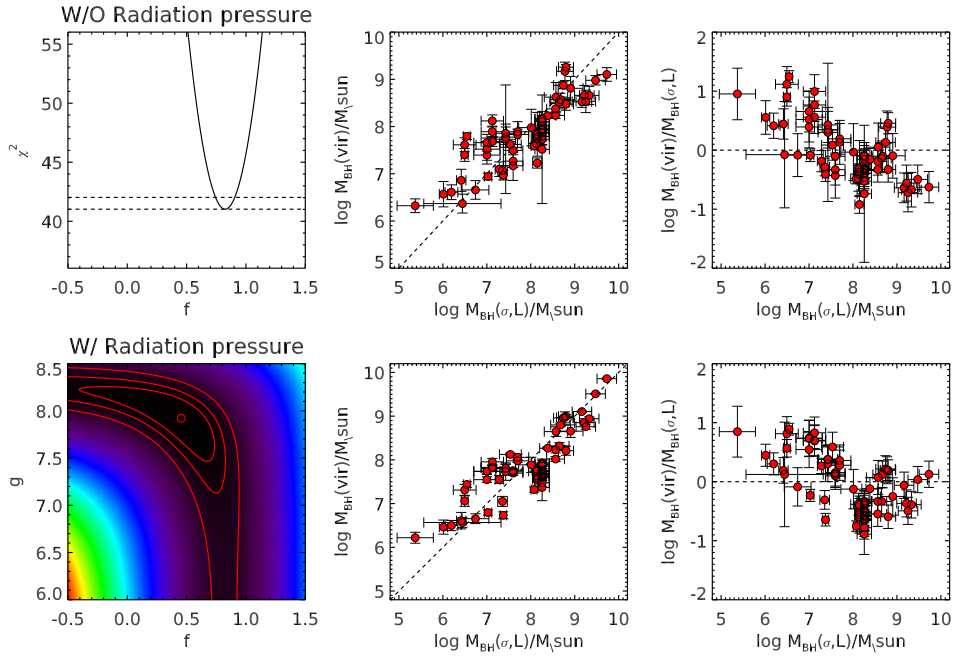

Figure 4.2 Calibration of RM virial masses from Hβ using $\sigma(rms)$. Top and bottom panels in figure represent the cases without and with radiation pressure, respectively. Central and right panels compare $M_{\rm BH}(RM)$ vs $M_{\rm BH}(\sigma, L)$ (center) and their ratio vs $M_{\rm BH}(\sigma, L)$. The top left panel presents the χ^2 value for the variation of f in the case of no radiation pressure; the dashed horizontal lines represent the minimum χ^2 and 1σ values. In the lower left panel, the image represents the χ^2 value for the joint variation of f and g, the circle the minimum χ^2 value while the contours represent $\Delta\chi^2_{min} + [2.30, 4.61, 9.21]$, i.e. the 68%, 90%, 99% confidence contours for two significant parameters (Avni 1976). Note the different values of f in the two cases.

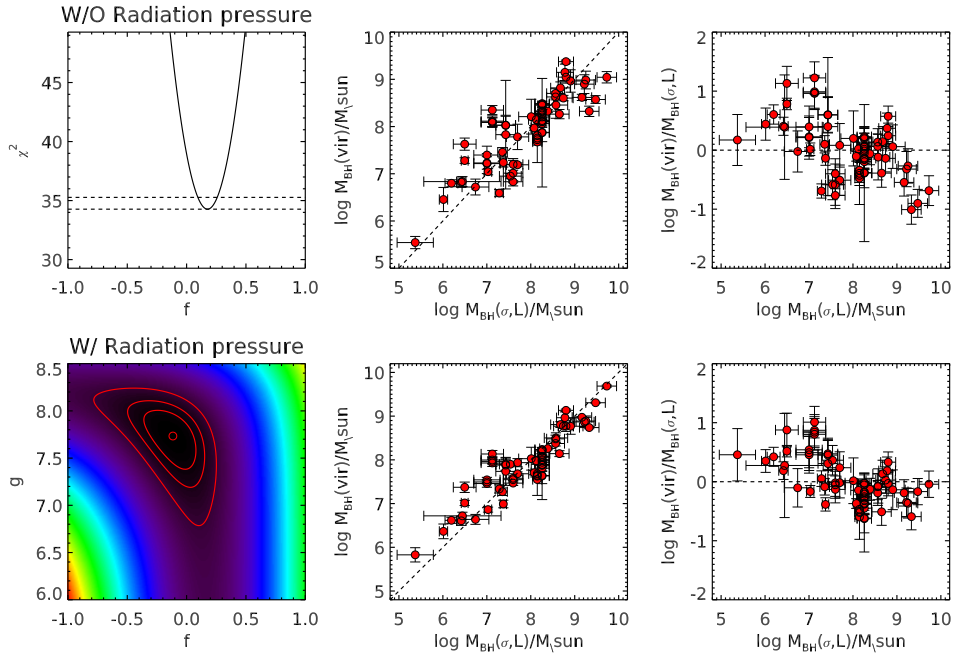

Figure 4.3 Calibration of RM virial masses from Hβ using $FWHM(mean)$. Top and bottom panels in figure represent the cases without and with radiation pressure, respectively. Central and right panels compare $M_{\rm BH}(RM)$ vs $M_{\rm BH}(\sigma,L)$ (center) and their ratio vs $M_{\rm BH}(\sigma,L)$. The top left panel presents the χ^2 value for the variation of f in the case of no radiation pressure; the dashed horizontal lines represent the minimum χ^2 and 1σ values. In the lower left panel, the image represents the χ^2 value for the joint variation of f and g, the circle the minimum χ^2 value while the contours represent $\Delta\chi^2_{min}+[2.30,4.61,9.21]$, i.e. the 68%, 90%, 99% confidence contours for two significant parameters (Avni 1976). Note the different values of f in the two cases.

Table 4.1 Calibration of virial masses from reverberation mapping (RM) or single epoch observations (SE). Rows with $g = -10$ (fixed) correspond to cases without the radiation pressure correction.

Line	$V_{\rm BLR}$	$R_{\rm BLR}$	f	g	$\sigma_{\rm res}$ [a]	$\sigma_{\rm int}$ [b]
Hβ (RM)	$\sigma(rms)$	$c\tau_{cen}$	0.45 (+0.28, -0.85)	7.92 (+0.33, -0.45)	0.49	0.43
			0.83 (+0.07, -0.08)	-10*	0.48	0.42
Hβ (RM)	$FWHM(mean)$	$c\tau_{cen}$	-0.12 (+0.19, -0.24)	7.73 (+0.26, -0.35)	0.40	0.31
			0.18 (+0.08, -0.08)	-10*	0.48	0.41
Hβ (SE)	$FWHM(mean)$	$\propto L_{5100}^{0.5}$	6.63 (+0.20, -0.28)	7.82 (+0.25, -0.31)	0.43	0.36
			6.97 (+0.07, -0.07)	-10*	0.50	0.44
Mg II (SE)	$FWHM(SE)$	$\propto L_{3000}^{0.5}$	6.85 (+0.18, -0.21)	7.27 (+0.33, -0.50)	0.44	0.33
			6.82 (+0.09, -0.11)	-10*	0.50	0.37
C IV (SE)	$FWHM(SE)$	$\propto L_{1350}^{0.5}$	6.48 (+0.24 -0.34)	7.33 (+0.29, -0.41)	0.51	0.50
			6.80 (+0.09, -0.09)	-10*	0.62	0.61

[a] *r.m.s.* of the residuals computed for the f, g values of minimum χ^2.
[b] Intrinsic dispersion of the residuals (i.e. removing contribution from measurement errors).
* Fixed fit parameter.

mass estimator

$$M_{\rm BH}(SE)/{\rm M}_\odot = 10^f \left(\frac{FWHM(mean)}{1000\,{\rm km\,s^{-1}}}\right)^2 \left(\frac{L_{5100}}{10^{44}\,{\rm erg\,s^{-1}}}\right)^{0.5} + 10^g \left(\frac{L_{5100}}{10^{44}\,{\rm erg\,s^{-1}}}\right) \quad (4.8)$$

$$(4.9)$$

the calibration procedure is the same which has been followed in the RM case. Results are shown in fig. 4.4 and table 4.1. First, the use of L_{5100} as a proxy for the BLR radius does not decrease the accuracy of $M_{\rm BH}(SE)$ w.r.t. $M_{\rm BH}(RM)$ when compared to $M_{\rm BH}(\sigma, L)$: the r.ms. and intrinsic dispersions of the residuals are similar. Second, we find again an improvement by 0.1 dex in intrinsic dispersion, when taking into account the correction for radiation pressure as it can be clearly seen in the figure.

Overall, it seems that using SE virial masses we can estimate the true masses with an accuracy ~ 0.36 dex in log (1σ).

The SE virial mass estimator for Hβ is therefore

$$M_{\rm BH}({\rm H}\beta, SE)/{\rm M}_\odot = 10^{6.63\,(+0.20,-0.28)} \left(\frac{FWHM(mean)}{1000\,{\rm km\,s^{-1}}}\right)^2 \left(\frac{L_{5100}}{10^{44}\,{\rm erg\,s^{-1}}}\right)^{0.5} + 10^{7.82\,(+0.25,-0.31)} \left(\frac{L_{5100}}{10^{44}\,{\rm erg\,s^{-1}}}\right) \quad (4.10)$$

4.5 Calibration of $M_{\rm BH}$ based on Mg II and on C IV

To calibrate SE virial masses based on Mg II we use the measurements from SE spectra obtained with IUE or HST/STIS of the galaxies in the RM database performed by Wang et al. (2009) (their table 1). As previously we also use the average per-object values in order to check that the non equal number of measurement per object affect the results. We assume a 0.5 slope for the radius-luminosity relation. The results are shown in Fig. 4.5 and table 4.1. Compared to Hβ, the correction for radiation pressure is smaller and less

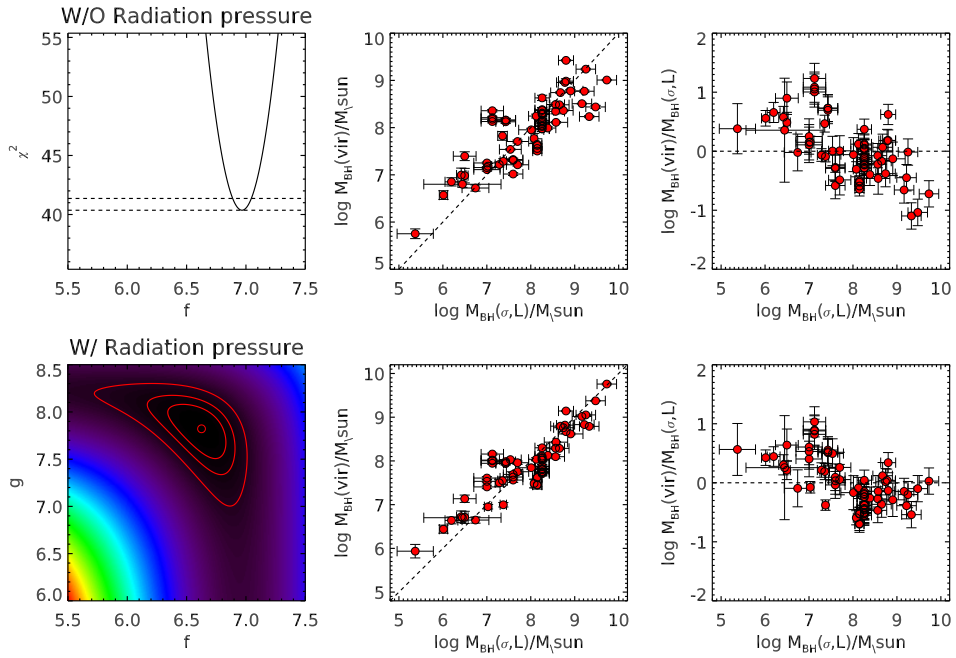

Figure 4.4 Calibration of SE virial masses from Hβ. Top and bottom panels in figure represent the cases without and with radiation pressure, respectively. Central and right panels compare $M_{\rm BH}(RM)$ vs $M_{\rm BH}(\sigma,L)$ (center) and their ratio vs $M_{\rm BH}(\sigma,L)$. The top left panel presents the χ^2 value for the variation of f in the case of no radiation pressure; the dashed horizontal lines represent the minimum χ^2 and 1σ values. In the lower left panel, the image represents the χ^2 value for the joint variation of f and g, the circle the minimum χ^2 value while the contours represent $\Delta\chi^2_{min}+[2.30,4.61,9.21]$, i.e. the 68%, 90%, 99% confidence contours for two significant parameters (Avni 1976). Note the different values of f in the two cases.

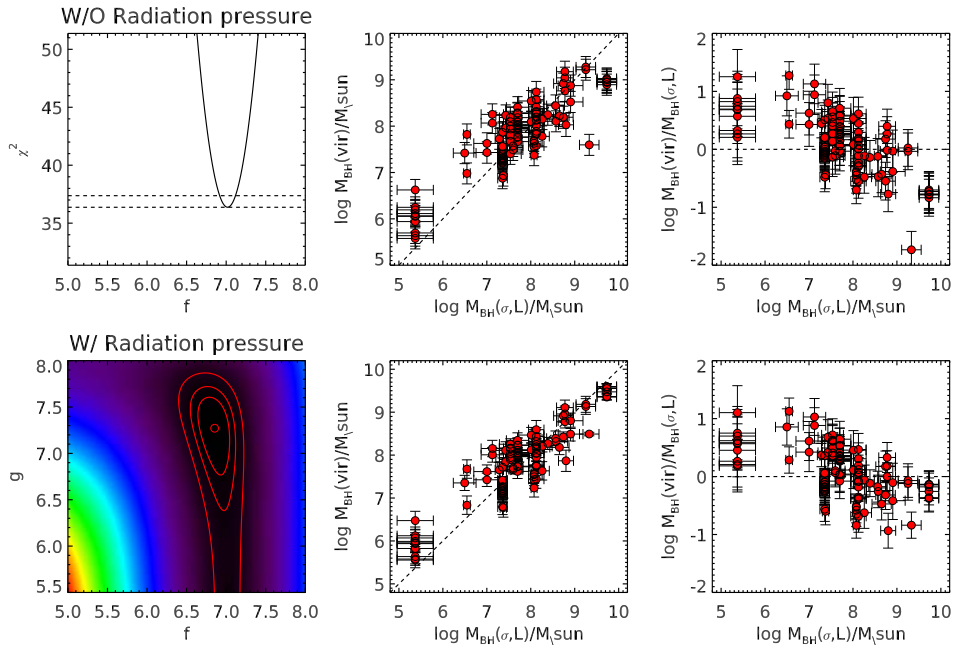

Figure 4.5 Calibration of SE virial masses from Mg II Top and bottom panels in figure represent the cases without and with radiation pressure, respectively. Central and right panels compare $M_{\rm BH}(RM)$ vs $M_{\rm BH}(\sigma,L)$ (center) and their ratio vs $M_{\rm BH}(\sigma,L)$. The top left panel presents the χ^2 value for the variation of f in the case of no radiation pressure; the dashed horizontal lines represent the minimum χ^2 and 1σ values. In the lower left panel, the image represents the χ^2 value for the joint variation of f and g, the circle the minimum χ^2 value while the contours represent $\Delta\chi^2_{min}+[2.30,4.61,9.21]$, i.e. the 68%, 90%, 99% confidence contours for two significant parameters (Avni 1976). Note the different values of f in the two cases.

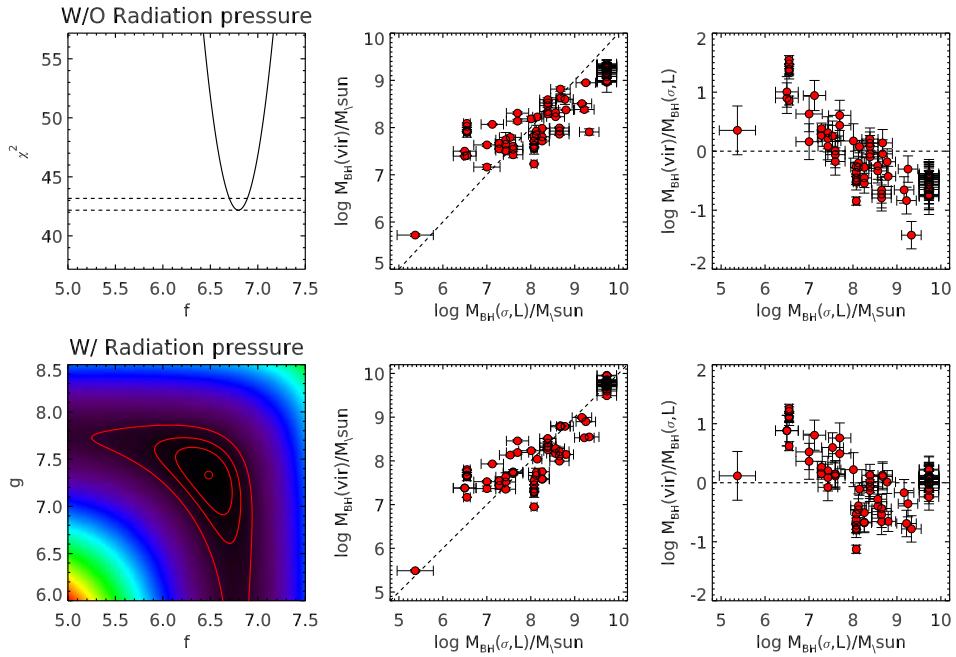

Figure 4.6 Calibration of SE virial masses from C IV Top and bottom panels in figure represent the cases without and with radiation pressure, respectively. Central and right panels compare $M_{\rm BH}(RM)$ vs $M_{\rm BH}(\sigma,L)$ (center) and their ratio vs $M_{\rm BH}(\sigma,L)$. The top left panel presents the χ^2 value for the variation of f in the case of no radiation pressure; the dashed horizontal lines represent the minimum χ^2 and 1σ values. In the lower left panel, the image represents the χ^2 value for the joint variation of f and g, the circle the minimum χ^2 value while the contours represent $\Delta\chi^2_{min}+[2.30, 4.61, 9.21]$, i.e. the 68%, 90%, 99% confidence contours for two significant parameters (Avni 1976). Note the different values of f in the two cases.

important. Correcting for an average $\log L_{3000}/L_{5100} \sim 0.2$ dex (see below), this means that $g(MgII)$ is about 0.35 dex smaller than $g(\mathrm{H}\beta)$, and this can be attributed to a difference in $N_{\rm H}$ meaning that the average $N_{\rm H}$ of Mg II-emitting clouds is 0.35 dex larger than that of Hβ-emitting clouds (we will return to this issue later). Since the correction for radiation pressure is smaller, it is not surprising that there is almost no difference in the residuals when using or not the correction for radiation pressure. Even in this case the intrinsic dispersion of the residuals is relatively low, ~ 0.35 dex.

Finally, we calibrate SE virial masses based on C IV using the measurements from SE spectra by Vestergaard & Peterson (2006). In particular, following Vestergaard & Peterson (2006), we consider their database of single epoch measurements of FWHM(C IV) and L_{1350} (λL_λ at

1350Å) and we discard three measurements (out of 85) which have an error close to 50% on line widths. As previously we also use the average per-object values in order to check that the non equal number of measurement per object affect the results. We assume a 0.5 slope for the radius-luminosity relation. The results are shown in Fig. 4.6 and table 4.1. The intrinsic dispersion of the residuals is ~ 0.5 dex when including the correction for radiation pressure, slightly larger than has been found for Hβ and Mg II. This increases by 0.1 dex when neglecting radiation pressure.

4.6 Line width vs continuum luminosity distributions: data

We now verify the effects of the calibrations performed above and in particular we try to assess whether we can explain behaviours and how BH masses from different lines are affected.

We use the results of the line fitting performed in Chapter 3 on quasars from the Seventh and Tenth Data Releases of the Sloan Digital Sky Survey (SDSS). In particular, we consider the line widths and continuum luminosities for Hβ and Mg II. When available, we also consider the same quantities for C IV from Shen et al. (2011), whose results are only restricted to DR7. We first select all spectra with simultaneous observations of Hβ and Mg II, using a S/N threshold of 3.

In figure 4.7a we compare the luminosities of the 5100 and 3000Å continua, adjacent to Hβ and Mg II, respectively. There is a small non linearity in the relation among continuum luminosities. By fitting the red points (see figure) we obtain:

$$\log L_{3000} = (0.945 \pm 0.001) + (1.07 \pm 0.03)(\log L_{5100} - 0.75) \tag{4.11}$$

this non linearity corresponds to a change of the spectral slope with luminosity.

In figure 4.7b we compare the FWHM of Hβ and Mg II. A striking feature is the non linearity of the relations between the FWHM of Hβ and Mg II. The solid line in the figure corresponds

to the relation

$$\log W_{\mathrm{Mg\,II}} = (3.537 \pm 0.002) + (0.646 \pm 0.007)(\log W_{\mathrm{H}\beta} - 3.7) \tag{4.12}$$

given the considerable intrinsic dispersion in the relation, one has also to consider the fit results when exchanging x with y, which provides a slope for the above relation of 0.934 ± 0.009. The bisector is therefore still well below a linear relation.

This non linear relation results in a non linear relation between virial BH masses estimated from Hβ and Mg II. Such non linear relations is not simply explained in a framework which neglects radiation pressure. Onken & Kollmeier (2008) corrected for this effect empirically but do not provide any physical explanation for its origin.

This non-linear relation is present in other works presented in the literature like Shen et al. (2008) , Vestergaard & Osmer (2009) (LBQS quasar sample) and McGill et al. (2008) (lower luminosity Seyferts selected from SDSS). In particular, the data by Vestergaard & Osmer (2009) and McGill et al. (2008) show the same non -linearity. This does not exclude systematic effects due to the adopted Fe II template in the fitting of line profiles.

Regarding the comparison between Mg II and C IV lines and their continua, refer to figure 4.8. There is no relation among line widths, but a linear relation among continuum luminosities which we fit as

$$\log L_{1350} = (2.187 \pm 0.002) + (0.949 \pm 0.006)(\log L_{3000} - 2.00) \tag{4.13}$$

4.7 Line width vs continuum luminosity distributions: model and observations

Emission line widths ($V = \log[FWHM/(1000\,\mathrm{km/s}]$) and adjacent continuum luminosities ($L = \log[\lambda L_\lambda/(10^{44}\,\mathrm{erg/s})]$) are the two available observables which encode the structure and kinematics of the BLR. Given a large sample of objects, the morphology of the observed LV

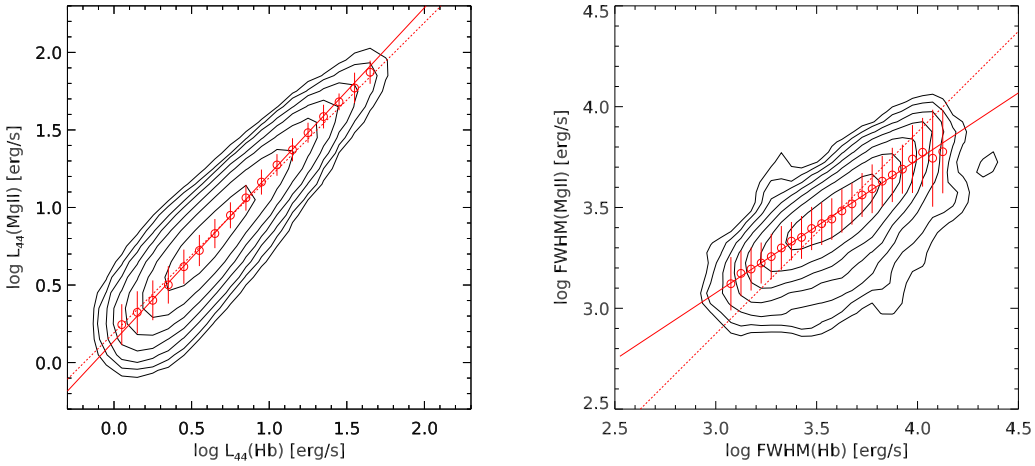

Figure 4.7 Left panel: 3000 Å vs 5100 Å continuum luminosities. The observed distribution was obtained with $\Delta L = 0.05$ dex luminosity bins, and smoothed by convolving with a Gaussian function with FWHM = 0.1 dex (2 pix). The red dots denote the median 3000Å luminosities per given 5100Å bin, the error bars the percentiles (16%, 84%) choses such that the total bar include 68% of the points in each bin. The solid red line is the best linear fit to the red dots (as errors we have used the bars divided by the square root of the number of points) which has slope ~ 1.1. For comparison, the dashed red line is the linear relation $L_{3000} = 10^{0.2} L_{5100}$. Right panel: Comparison of Hβ and Mg II line widths. The observed distribution was obtained with $\Delta V = 0.1$ dex velocity bins, and smoothed by convolving with a Gaussian function with FWHM = 0.2 dex (2 pix). Red points and lines are as in the left panel. The dashed red line is the linear relation $FWHM_{\rm Mg\,II} = 10^{-0.2} FWHM_{\rm H\beta}$.

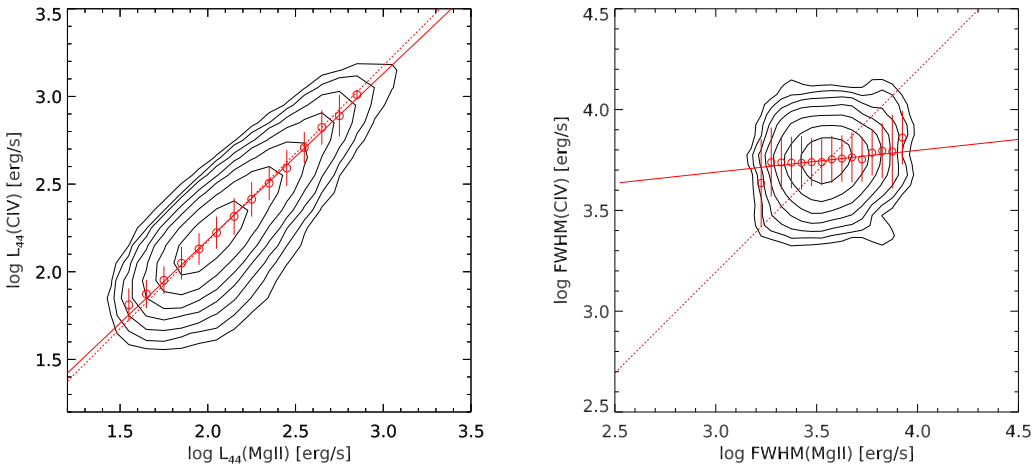

Figure 4.8 Same as Fig. 4.7 but for C IV and Mg II.

distribution can provide indications on the BLR structure and kinematics. In particular, the comparison among *LV* diagrams from different emission lines originating from the same sample of objects can provide indications on the relative differences between the line emitting regions. It is there that one must seek for evidences for radiation pressure force effects, if any.

Two lines, labeled as 1 and 2, are characterized by two observed *LV* diagrams which provide probability distributions $P(L_1,V_1)$ and $P(L_2,V_2)$, respectively. In any given object L_1,V_1 and L_2,V_2 must be connected through the geometrical and kinematical structure of the BLR. Therefore, in any sample composed of objects where L_1,V_1 and L_2,V_2 can be measured simultaneously, it should be possible to write, by the Bayes theorem,

$$P(L_2,V_2) = \int\int dL_1 dV_1\, P(L_2,V_2|L_1,V_1)P(L_1,V_1) \tag{4.14}$$

where $P(L_1,V_1)$ and $P(L_2,V_2)$ are the LV probability distributions for lines 1 and 2 respectively (i.e. the probability distributions which are observed) and $P(L_2,V_2|L_1,V_1)$ is the conditional probability distribution of L_2,V_2 for any given L_1,V_1 values. The $P(L_2,V_2|L_1,V_1)$ conditional distribution provides the connection between L_2,V_2 and L_1,V_1, that is the connection between geometry and kinematics of line 1 and 2. Assuming that there is no direct relation between L and V one can separate variables by writing

$$P(L_2,V_2|L_1,V_1) = F[L_2-\bar{L}_2(L_1,V_1)]G[V_2-\bar{V}_2(L_1,V_1)] \tag{4.15}$$

where $\bar{L}_2(L_1,V_1)$ and $\bar{V}_2(L_1,V_1)$ are functions providing the average expected values for L_2 and V_2 for any given set of values L_1,V_1. Then $F[]$ and $G[]$ are the probability distributions of the observed L_2, V_2 around the expected average values. Their most simple form is either a Dirac's delta or a Gaussian, with the former indicating the ideal case of no intrinsic dispersion and the latter allowing for a more realistic dispersion around the expected average values. If the continuum luminosity has a power law dependence of energy ($L_\nu \sim \nu^{-\alpha}$) then

$$\bar{L}_2(L_1,V_1) = \beta L_1 + \gamma \tag{4.16}$$

with $\gamma = (1-\alpha)\log(\nu_2/\nu_1)$. β allows for non log-linear relations, like the ones between the continuum luminosities at 3000 and 5100Å.

By assuming that the BLR is virialized one can then write

$$M_{\rm BH} = 10^{(f_1+2*V_1+a_1*L_1)} + 10^{(g_1+L_1)} \quad (4.17)$$

$$M_{\rm BH} = 10^{(f_2+2*V_2+a_2*L_2)} + 10^{(g_2+L_2)} \quad (4.18)$$

where $M_{\rm BH}$ is the BH mass which is the same for line 1 and 2. Considering eq. 4.18 and substituting L_2 with its expected average value $\bar{L}_2$ from eq. 4.16 one can trivially derive V_2 as a function of L_1, V_1, that is the $\bar{V}_2(L_1, V_1)$ function

$$\bar{V}_2(L_1, V_1) = \frac{1}{2}\left[\log\left(M_{\rm BH} - 10^{(g_2+L_1+\gamma)}\right) - f_2 - a_2(L_1+\gamma)\right] \quad (4.19)$$

with $M_{\rm BH}$ given by eq. 4.17. If the above assumptions are correct it should be possible to reproduce the observed $P(L_2, V_2)$ distribution starting from the observed $P(L_1, V_1)$ one. Given the calibration of virial masses for line 1, the free parameters are therefore

- f_2, g_2, a_2, γ, σ_γ, σ_V

where σ_γ and σ_V are the standard deviations of the $F[L_2 - \bar{L}_2(L_1, V_1)]$ and $G[V_2 - \bar{V}_2(L_1, V_1)]$ functions which are assumed to be Gaussian. These free parameters can be determined by minimizing the differences between the $P(L_2, V_2)$ distribution derived from line 1 and the observed one. In practice, with $P_2 = P(L_2, V_2)$ and $\tilde{P}_2 = \tilde{P}(L_2, V_2; f_2, g_2, a_2, \gamma, \sigma(\gamma), \sigma(V))$ we minimize

$$\chi^2 = \sum_i \frac{(P_{2,i} - \tilde{P}_{2,i})^2}{\tilde{P}_{2,i}} \quad (4.20)$$

where the index i refers to the values in $i-th$ bin in the LV plane which we have used to derive the observed distributions. $\tilde{P}_{2,i}$ at the denominator is the square of the poissonian error. The sum is of course extended only to the bins with non-null $\tilde{P}_{2,i}$ values.

4.7.1 Comparison of Mg II and Hβ LV distribution

As described above, we consider our fits to the quasars spectra from DR 7 and DR 10 of the SDSS which are described in Chapter 3. In order to calibrate Mg II and compare it with Hβ, we selected all quasars in the redshift range $0.4 \lesssim z \lesssim 0.9$, whose SDSS spectra contain both Hβ and Mg II and have an average pixel by pixel signal-to-noise is $S/N > 3$.

We selected bin sizes of 0.2 dex for continuum luminosity and 0.04 dex for FWHM and we considered the ranges $[43.5, 47.4]$ and $[3.1, 4.3]$ for luminosities and logarithmic line widths respectively. The results of the fits are shown in table 4.2 and fig. 4.9.

The L, V distribution of Mg II is not compatible with that of Hβ in the classic (no radiation pressure case). The reduced χ^2 (3.2) is almost a factor 2 worse than in the case with radiation pressure (1.6) which has only one free parameter more. The reason should be that the distribution of FWHM is broader for Hβ than Mg II and this cannot be accounted for in the classic virial case. Conversely, in the radiation pressure case the narrower distribution of Mg II line widths can be accounted for by the negligible importance of radiation pressure for Mg II emitting clouds compared to Hβ emitting clouds. Note that the derived value of f_2 in this case corresponds to a negligible effect of radiation pressure.

Given the results of the best fit and using the formalism of the previous section we can easily compare observed and expected VV distributions from the LV Hβ distribution. This is done in figure 4.10. There is a nice agreement in the case with radiation pressure, but not in the case without radiation pressure were the expected VV distribution is more extended along the 1:1 line and tilted in the opposite direction. The non linearity in the VV relation is then explained in terms of the radiation pressure effect. For MgII emitting clouds radiation pressure is always negligible. In most of the Hβ objects with large FWHM radiation pressure has also limited importance. Radiation pressure is important in the objects with larger MgII FWHM for given Hβ. In practice radiation pressure rotate upwards the VV distribution pivoting around [3.9,3.8]. This is shown by the right panel where we consider only the distribution of objects which are not significantly affected by radiation pressure: defining $\xi = M_{BH,rad}/M_{\rm BH}$ ($M_{BH,rad}$ is the correction for radiation pressure to obtain the total BH mass)

Table 4.2 Best parameters which are then used to derive the observed $P(L,V)$ distribution of Mg II from Hβ.

Classic case (no radiation pressure)

f_1	g_1	a_1	f_2	g_2	a_2	γ	σ_γ	σ_V	χ^2/dof	Notes
6.97*	-10.0*	0.5*	7.12	-10.0*	0.5	0.0*	0.14	0.02	414 / 78	a

Case with radiation pressure

f_1	g_1	a_1	f_2	g_2	a_2	γ	σ_γ	σ_V	χ^2/dof	Notes
6.63*	7.82	0.5*	7.00	7.52	0.5	0.0*	0.17	0.11	165 / 85	a

*Fixed fit parameter.
a) $\Delta L = 0.1$, $\Delta V = 0.05$, $S/N \geq 3$ where ΔL and ΔV are the logarithmic bin sizes (dex) for luminosities and FWHM, S/N is the cutoff value for spectra selection.

and considering objects for which $\log \xi < -0.5$, we find that the VV relation is linear.

We now compare virial BH mass estimates from Hβ and Mg II in view of our new calibration (Fig. 4.11). BH masses estimated without taking into account radiation pressure exhibit a non linear relation, which is the result of the non linearity between FWHM of Hβ and Mg II. Conversely, when radiation pressure is taken into account this non linearity disappears entirely. Moreover as shown in the histogram of the $M_{\rm BH}({\rm Mg\,II})/M_{\rm BH}({\rm H}\beta)$ values, the rms dispersion decreases by $\sim 25\%$ (0.24 vs 0.31 dex).These results confirm the validity of the radiation pressure correction applied to Hβ only.

4.7.2 Comparison of Mg II and C IV LV distributions

In this section we compare Mg II and C IV on the basis of the calibrations performed in the previous sections, considering only the sources where both C IV and Mg II fall the observed spectral range. For C IV line width and continuum luminosity we use the results of the fits by Shen et al. (2011).

In figure 4.12 we compare the observed LV diagrams of MgII with those expected from C IV. The results of the comparison are summarized in Tab. 4.3. There is a fair agreement in both cases, with a smaller χ^2 in the case without radiation pressure. The agreement is worse than

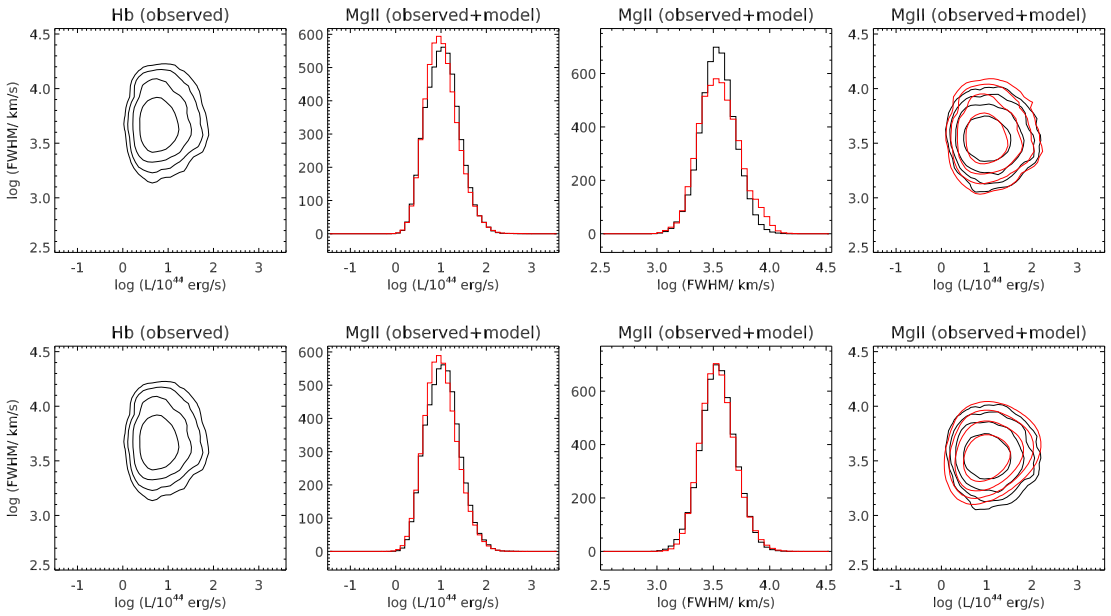

Figure 4.9 Top panels: observed and model *LV* distributions for the case without radiation pressure. The left panel is the observed *LV* distribution for Hβ. The central panels compare the observed continuum luminosity and width distributions for Mg II (black histograms) with those expected from Hβ and computed as described in the text. Finally the right panel compare the observed *LV* distribution for Mg II with the one expected from Hβ. Black lines represent observed quantities, red lines represent model ones. Bottom panels: same as top panels for the case with radiation pressure.

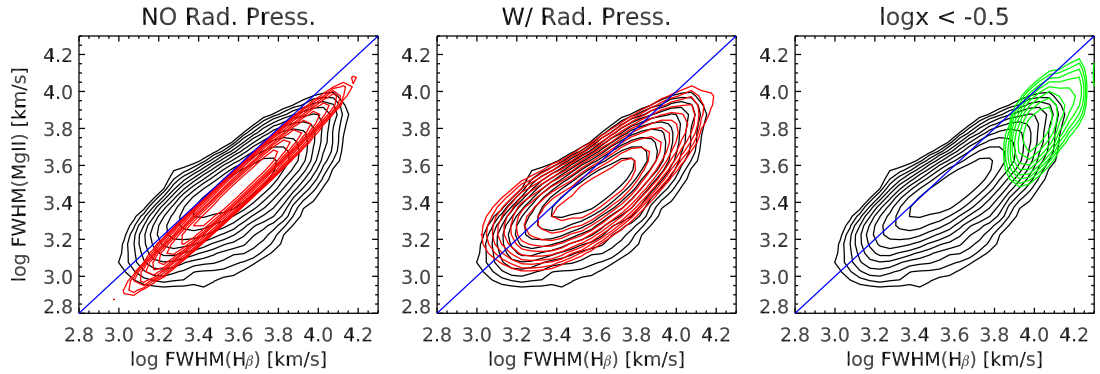

Figure 4.10 Comparison of observed *VV* distributions for Mg II and Hβ (black lines) with expectations from Hβ only in the cases of no radiation pressure (left panel), radiation pressure correction (center panel) and objects with negligible contribution of radiation pressure (right panel, see text). Black lines represent observed quantities, red and green lines represent model ones.

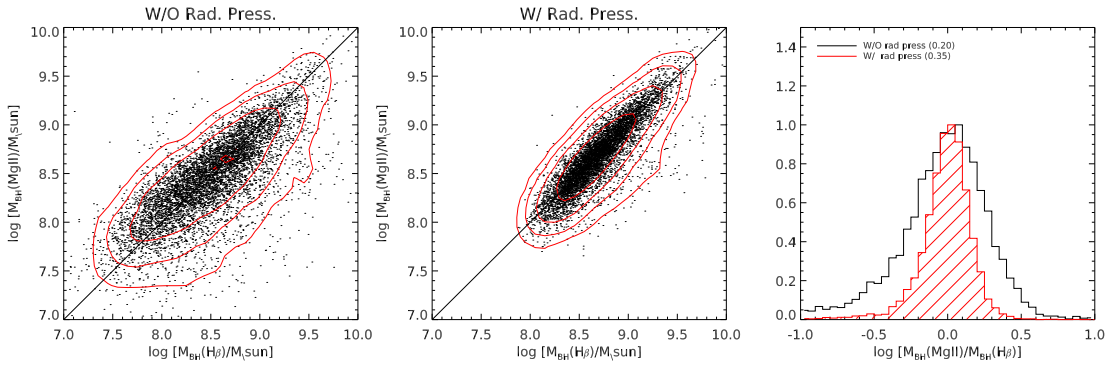

Figure 4.11 Comparison between virial BH masses derived from Hβ and Mg II in the cases of no radiation pressure correction (left), radiation pressure correction (center). The red contours represent constant number density levels and are only shown to guide the eye. In the right panel we compare the ratio between the two BH mass estimates in the cases with and without radiation pressure (the numbers in parenthesis are the rms dispersion of the histograms).

in the comparison of Hβ and Mg II.

In figure 4.13, we compare the observed VV relation between C IV and Mg II with the expected one. The observed distribution shows a clear absence of any relation between the observed FWHM of Mg II and C IV. This is in sharp contrast with what one expects in the classic case, i.e. without radiation pressure. This has prompted many authors to question the reliability of $M_{\rm BH}$ estimates based on C IV. However, when radiation pressure is taken into account, the expected relation between Mg II and C IV is much broader than, e.g., the one between Mg II and Hβ. Although the expected VV relation for Mg II and C IV does not reproduce the observed one, it has a much better agreement than in the case without radiation pressure. This suggests that C IV is indeed affected by outflows but probably not at a level which would entirely jeopardise the relation between Mg II and C IV FWHM.

Finally, in figure 4.14 we compare BH masses expected from C IV and Mg II. In the case without radiation pressure there is a broad tail of objects with large BH mass in Mg II compared to C IV. This tail disappears completely when correcting for radiation pressure of C IV. The disappearance of the tail results in a smaller rms of the $M_{\rm BH}$(Mg II)/$M_{\rm BH}$(C IV) which goes from 0.42 to 0.32 dex.

Table 4.3 Best parameters to derive the observed $P(L,V)$ distribution of C IV from Mg II.

Classic case (no radiation pressure)

f_1	g_1	a_1	f_2	g_2	a_2	γ	σ_γ	σ_V	χ^2/dof	Notes
7.12*	-10.0*	0.50*	6.64*	-10.0*	0.50*	0.0*	0.10	0.05	157 / 72	a

Case with radiation pressure

f_1	g_1	a_1	f_2	g_2	a_2	γ	σ_γ	σ_V	χ^2/dof	Notes
7.00*	7.52*	0.50*	6.72	7.3	0.71*	0.0*	0.16	0.10	265 / 89	a

*Fixed fit parameter.
a) $\Delta L = 0.1$, $\Delta V = 0.05$, $S/N \geq 3$ where ΔL and ΔV are the logarithmic bin sizes (dex) for luminosities and FWHM, S/N is the cutoff value for spectra selection.

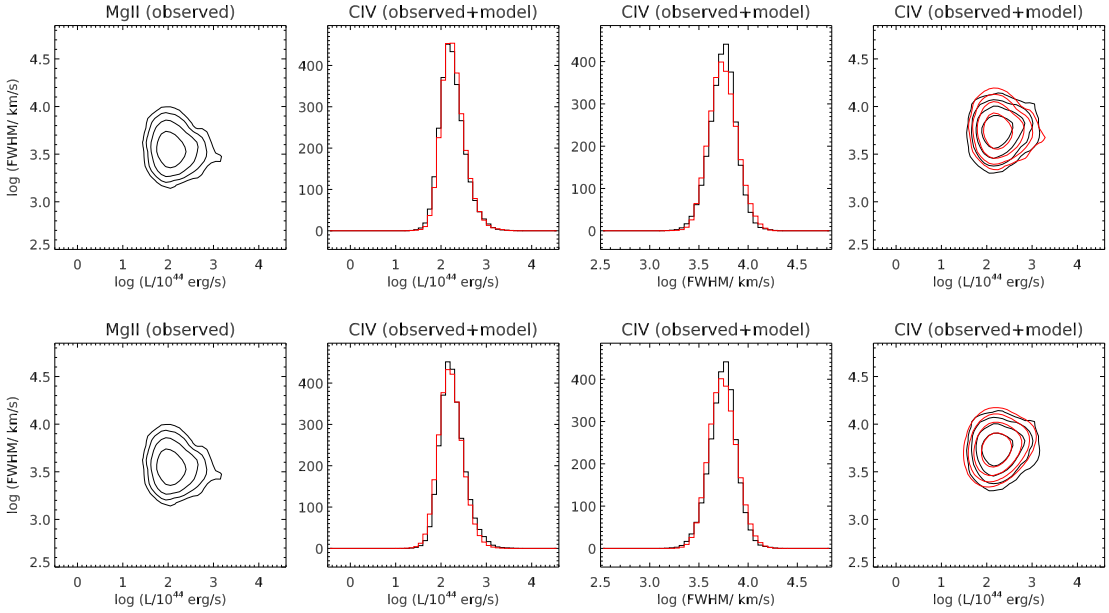

Figure 4.12 Top panels: observed and model LV distributions for the case without radiation pressure. The left panel is the observed LV distribution for Mg II. The central panels compare the observed continuum luminosity and width distributions for C IV (black histograms) with those expected from Mg II and computed as described in the text. Finally the right panel compare the observed LV distribution for C IV with the one expected from Mg II. Bottom panels: same as top panels for the case with radiation pressure.

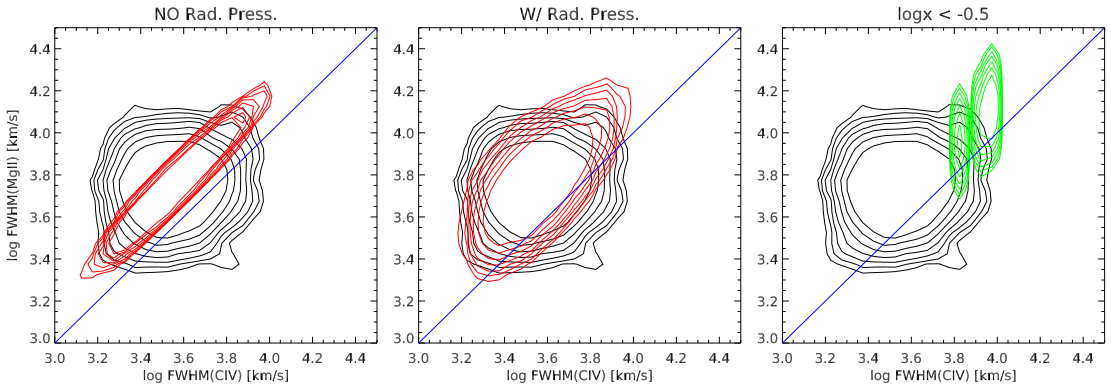

Figure 4.13 Comparison of observed VV distributions for Mg II and C IV (black lines) with expectations from Mg II only in the cases of no radiation pressure (left panel), radiation pressure correction (center panel) and objects with negligible contribution of radiation pressure (right panel).

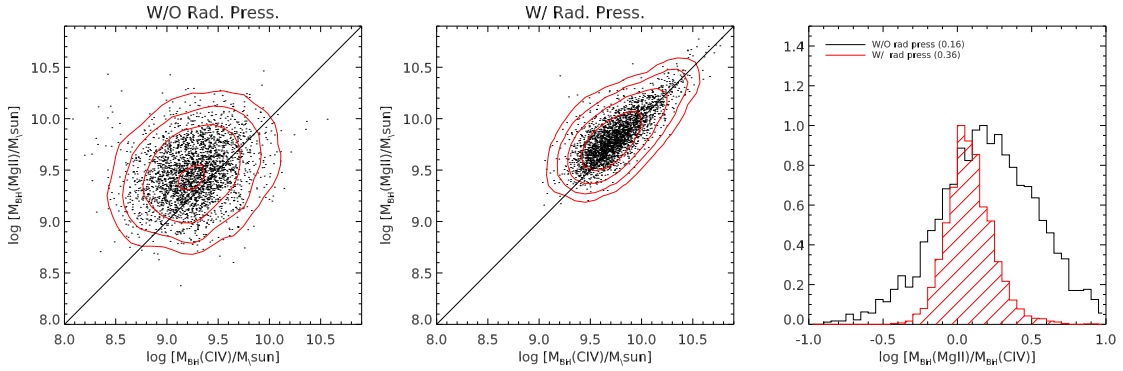

Figure 4.14 Comparison between virial BH masses derived from C IV and Mg II in the cases of no radiation pressure correction (left), radiation pressure correction (center). The red contours represent constant number density levels and are only shone to guide the eye. In the right panel we compare the ratio between the two BH mass estimates in the cases with and without radiation pressure (the numbers in parenthesis are the rms dispersion of the histograms).

4.8 A coherent physical picture

We hereby propose a coherent physical picture on BLR line profiles and the effect of radiation pressure, based on the results presented in the previous sections.

We start by assuming that line profiles vary with varying radiation pressure: when the radiation pressure is important the profile has extended wings and is spiky (Pop A), conversely when radiation pressure is not important the profile is bell shaped (Pop B). The importance of radiation pressure is set by the ratio between the radiation pressure correction and the virial term which is indeed proportional to the quantity which has been used in the literature as Eddington ratio (see, e.g., figure 4.1) and which we label as $(L/L_{\rm Edd})_{lit}$. $(L/L_{\rm Edd})_{lit}$ is computed using BH masses without radiation pressure correction and therefore is proportional to the ratio between the radiation pressure correction and the virial term. The true $(L/L_{\rm Edd})$ ratio should be computed using radiation pressure corrected virial masses.

$(L/L_{\rm Edd})_{lit}$ – which has also been suggested as the driver for Eigenvector I – identifies a sequence of line profiles which vary smoothly from spiky to bell shaped. As a consequence there is a non linearity between FWHM and σ of broad emission lines, which just reflects profile variations driven by radiation pressure. The use of σ to estimate virial BH masses might bias the estimate because of the presence of the wings due to outflowing material. In practice, when using σ one is somehow already taking into account radiation pressure, since for a given $M_{\rm BH}$, lines at large L have larger σ than they would have following a pure virial relation due to the presence of the broad wings. To calibrate virial masses it is therefore better to use FWHM. In this case the use of the radiation pressure correction does significantly improve $M_{\rm BH}$ with respect to the no-correction case.

There is a (broad) distribution of column densities ($N_{\rm H}$) in BLR clouds and this means that lines with different excitations are characterized by different average $N_{\rm H}$. This is for instance the case of Hβ, C IV and Mg II. The different importance of radiation pressure explain the non-linear relation between the FWHM of Mg II and Hβ and the almost non-existent relation between the FWHM of Mg II and C IV. Finally we notice that the different corrections for radiation pressure found for Hβ, Mg II and C IV can be also explained with the different

line-weighted average column densities of the lines.

4.9 Conclusions

Virial BH masses derived by SE observations represent the only way to provide mass estimates for large samples of sources without demanding an excessive amount of telescope time. However, such measurements require an accurate calibration based on reverberation mapping data, in order to consistently represent a third rung in the so-called BH mass ladder. Previous works have profusely stressed this issue, debating about the need for a correction term that can take into account the effects of radiation pressure.

If we assume that BLR clouds have a non trivial distribution of column densities and if we also consider that the fluctuations in the AGN continuum luminosity, although rapidly affecting the ionisation state of BLR clouds, have much shorter timescales than BLR consequent structural rearrangements, there is no plausible reason why radiation pressure contribution to the AGN feedback should not be considered. On the contrary, radiation pressure can produce significant effects on broad line spectra and can explain the observative distinction between spiky and broad winged line profiles in Pop A and bell shaped profiles in Pop B AGN. Radiation pressure effects are also strongly dependent on the considered emission lines: those produced in high N_H clouds, which are less sensitive to ionising photons momentum deposition, do not frequently show such features.

Moreover, the already observed non-linear correlation between $FWHM$(mean) and σ(rms) of the Hβ line can be explained with a more significant sensitivity of σ (with respect to $FWHM$) to the broad wings in line profiles due to radiation pressure. By computing Eddington ratios (λ_{Edd}) without taking into account radiation pressure, for increasing λ_{Edd} line profiles tend to have larger σ for a given FWHM, in accordance with what is predicted for the transition from Pop B to Pop A sources, and also in accordance with our interpretation of broad winged profiles due to radiation pressure effects.

In order to quantify the effects of radiation pressure we started from calibrating BH masses from RM data and from SE spectra for the Hβ, Mg II and C IV broad emission lines. At

variance with all the previous works, we directly calibrate SE masses from $M_{\rm BH}(\sigma, {\rm L})$, without relying on RM calibrations. We consider the most recent measurements available for broad lines FWHM and σ both from mean and rms spectra, and using updated $M_{BH} - L_c/\sigma$ relations.

Our results for the calibration of BH masses from RM database show that, when using the velocity dispersion σ, an additional term due to radiation pressure has negligible effects on the inferred masses. On the contrary, the effects of radiation pressure are clearly seen when using the $FWHM$, with a decreased dispersion by 0.1 dex. This can be easily explained by noticing that σ may be more affected (with respect to $FWHM$) by eventual broad line wings produced by outflows and already includes the contribution of radiation pressure although in a way which cannot be easily quantified. Being also easier to measure and more stable with respect to the S/N of the spectra, $FWHM$ provides a much more reliable estimate of radiation pressure effects. Moreover, we also proved that, when including radiation pressure, BH masses derived by using FWHM and σ have the same accuracy.

Our calibration of SE virial masses showed that using continuum luminosity as a proxy to BLR size does not affect significantly the quality of measurements. Indeed by also including the radiation pressure term, the scatter decreases by 0.1 dex. FWHM appears therefore to be the best indicator of virial velocity, not only because it is more correlated with SE observations but also because it provides high quality mass measurements by also quantifying the effects of radiation pressure.

We also calibrated BH masses based on Mg II and C IV by using the available SE spectra of sources in the RM dataset. Mg II appears to be less sensitive to radiation pressure correction, with respect to Hβ, probably for its being mostly produced in high N_H clouds. BH masses calibration derived by C IV profiles show a high intrinsic dispersion, just mildly ameliorated by considering radiation pressure.

A first fundamental conclusion of this work is therefore a substantial differentiation of the broad lines response to radiation pressure: Mg II line does not show significant effects, C IV just moderately, while Hβ appears to be its best indicator.

In order to provide an even more solid evidence of the significant contribution of radiation

pressure on line profiles (and consequently on the inferred BH mass estimates), we investigated the probability density distribution of a large sample of quasars in the LV and VV diagrams. Line widths and continuum luminosities are indeed direct SE measures and, since BH mass estimates derived by different emission lines should in principle be equal, the corresponding LV and VV distributions should be correlated.

We used our line fitting results for a parent sample of SDSS quasars from the DR7Q and DR10Q database to infer from our results for the Hβ line the predicted LV diagram for Mg II, by assuming that $M_{BH}(\mathrm{H}\beta) = M_{BH}(\mathrm{Mg\,II})$. We then compare this prediction with the observed distribution, thus showing that by including radiation pressure the distributions are much more consistent. The corresponding VV distributions show a clear differential effect of radiation pressure on Hβ and Mg II, thus providing a solid explanation of the non-linearity of the observed V(Hβ)-V(Mg II) diagram.

We also derived a prediction of the LV and VV distributions for the C IV broad emission line from the observed Mg II diagrams. We find, in this case, an intrinsically larger prediction of the LV distribution. This result, combined with the larger dispersion predicted for the C IV R-L relation, shows that BH masses derived from C IV are much less reliable, even in the case of negligible feedback effects.

Chapter 5

General conclusions

The work here presented is part of the common effort to understand the physical processes defining the evolution of large scale structures in the Universe through the cosmic ages. Active Galactic Nuclei have been shown to represent fundamental witnesses of this evolution. Their structure and emission properties hide the proofs of the mutual influence between their host galaxies and their powerful internal engine, recognised to be supermassive black holes rapidly growing at the expense of the surrounding material.

The accretion process implies the formation of a typical structure around each SMBH, whose description is commonly referred to as to the Unified Model. Particular importance in this structure is assumed by the Broad Line Region, a compact cluster of clouds in rapid co-rotation and hosting dust grains beyond a certain grain sublimation distance from the BH.

The emission properties of the Broad Line Region, in particular its mean emissivity radius, can be used to infer BH masses with Reverberation Mapping techniques, but the latter are unfortunately extremely demanding in terms of observing time.

The observed correlation between the BLR mean emissivity radius and the continuum luminosity of active nuclei (R-L relation) appears then to be the only lifeline to let us collect mass estimates for large samples of sources with Single Epoch observations.

A complete understanding and an accurate calibration of the R-L relation is therefore mandatory. In particular, it is still unclear why an extremely variegated sample of sources can produce a rather tight correlation. In addition, it is a key issue to understand which are the

best emission lines to observe in order to have the minimum intrinsic dispersion of the R-L relation.

Our first work, here described in Chapter 2, intends to bridge this gap in the current understanding, by investigating the physical reasons for this fundamental correlation to arise. We used the photoionisation code CLOUDY to generate a very large number of cloud models, spanning over a wide range of electron density and incident flux of ionising radiation. This grid has been used to reproduce a BLR LOC model, thus deriving the integrated broad line emission and the mean emissivity radius for Hβ, Mg II and C IV.

We initially proved that the trivial model of a BLR extended up to the dust grain sublimation distance can perfectly explain the observed R-L relation. This simple model corresponds to the common assumption of the dust to be able to efficiently absorb all the ionizing photons, thus excluding the outer clouds contribution to the overall broad line emission.

Actually, by also including for BLR clouds to host dust grains beyond the sublimation distance, we demonstrated that dust surprisingly fails to reproduce what we called a *dusty wall*, and the predicted mean emissivity radius for a given continuum luminosity largely exceeds the observed values.

We also repeated our calculations by using the different approach of the CPE framework, finding again a not enough efficient absorption by dust grains.

The explanation we suggest for the efficiently broad line emitting clouds to be confined within a distance of the order of the sublimation radius is given by the optical depth of the clouds themselves, rapidly increasing at low ionization parameters and letting the self-shielding to prevent the ionizing radiation to reach farther distances. Optically thick clouds play therefore the role of a *wall* and define the internal boundary of the dust torus. It is indeed the existence of this boundary which ultimately defines the normalisation and the intrinsic dispersion of the R-L relation.

Another important finding of this work is that the presence of an outer boundary of the BLR also remarkably reduces the dependence of the mean emissivity radii on the geometric and structural parameters of the BLR, thus also explaining the tightness of the R-L relation even in the vast variety of the active nuclei.

Finally we proved that the Hβ and - even more - the Mg II broad emission lines provide the minimum intrinsic scatter of the R-L relation, and have therefore to be preferred for an accurate calibration of the Single Epoch BH mass measurements.
The results of the presented investigation will be submitted by the end of 2014 in the paper

- *"On the physical origin of the radius-luminosity relation in AGNs and the implications for the mass measurements of supermassive black holes"* by M. Sirigu, A. Marconi, H. Nezter, R. Maiolino and T. Nagao.

The observed optical-UV spectra of quasars can be used to derive virial BH masses and also unveil the effect of the feedback on the host galaxies, driven by outflows and radiation pressure.
The continuum luminosity can indeed be accurately measured only when all the other overlaying spectral features have been correctly removed and it is also clear that, on the other hand, feedback effects leave their footprints in quasar spectra that can be measured in terms of non-gaussian line profiles. It is nevertheless also obvious that the latter estimates can only be performed when extremely accurate line profiles and spectral decomposition are avalilable.
A second stage of the present work, described in Chapter 3 is therefore dedicated to a significant improvement in quasar spectral fitting, with respect to the current machinery. We considered the two largest quasar catalogs available as of today, SDSS-DR7Q and its latest extension, SDSS-DR10Q, and focused on the two fundamental spectral regions around the Hβ and Mg II broad lines.
We compared several fitting methods in order to correctly reproduce the continuum and its superimposed Fe IIemission. At the same time, we redefined the approach to each single component of the known spectral features in the considered wavelength range, with a spectra decomposition that is also more coherent with the general framework of physical processes originating them.
We thus produced a whole new spectral catalog of quasar properties for a very large sample

of sources, and compared our results for the DR7Q subsample with the ones previously published, confirming lower values of the χ^2/dof in every case.

Our new spectral fitting method has been applied to a third work, concerning the observable effects of radiation pressure on AGN spectra and BH mass measurements. In particular, quasar spectra provide a direct estimate of the continuum luminosity and of the virial velocity - in terms of the FWHM or the σ of the broad lines - to be used in SE BH mass estimates.
In addition, in order to take into account radiation pressure, it is necessary to consider an additional term to the trivial virial relation, which appears under reasonable assumption to be proportional to the continuum luminosity and inversely proportional to the column density.
Previous argumentations and even some recent direct measurements proved that BLR clouds are characterised by a broad distribution of N_H. This in turn means that the broad lines which are efficiently produced in the clouds with higher column density should be less sensitive to radiation pressure.
This work not only shows that feedback processes are indeed observable and ubiquitous but also provides a solid evidence of this differential response of broad emission lines to radiation pressure.
In order to achieve this fundamental result we started by deriving a new calibration of BH masses based on Hβ, Mg II and C IV for the sample of sources with RM mass measurements. For Hβ we found a non linear correlation of FWHM to σ. This result can easily be explained by considering that when radiation pressure becomes more important FWHM increases much more than σ, since the former is a much more efficient indicator of broad wings in line profiles due to outflows. This results in a broad distribution of FWHM measurements, with a certain degeneracy in the corresponding values of σ.
Our results for spectral fitting of the SDSS-DR7Q and SDSS-DR10Q quasars have then be used to better investigate the differential effects of feedback on broad emission lines and to ultimately prove the need for a correction factor in virial BH mass estimates.
By assuming that there is no direct connection between the continuum luminosity and the virial velocity estimated by the FWHM, we converted the observed distribution of Hβ spectra

in the LV diagram in a predicted distribution for Mg II and C IV and then compared such distributions to the observed ones. We also produced comparisons in the VV plane and in the BH mass distribution. What we found is that only taking into account the effects of radiation pressure we can correctly reproduce the observations.

This latter work will result in our second paper to be submitted in the first half of 2015:

- *"The effect of radiation pressure on virial black hole masses based on* Hβ*,* Mg II *and* C IV *broad emission lines"* by A. Marconi, M. Sirigu et al.

Bibliography

Abazajian, K. N., Adelman-McCarthy, J. K., Agüeros, M. A., et al. 2009, ApJS, 182, 543

Ahn, C. P., Alexandroff, R., Allende Prieto, C., et al. 2014, ApJS, 211, 17

Alexander, D. M., Swinbank, A. M., Smail, I., McDermid, R., & Nesvadba, N. P. H. 2010, MNRAS, 402, 2211

Allen, J. T., Hewett, P. C., Maddox, N., Richards, G. T., & Belokurov, V. 2011, MNRAS, 410, 860

Allende Prieto, C., Lambert, D. L., & Asplund, M. 2001, ApJL, 556, L63

Allende Prieto, C., Lambert, D. L., & Asplund, M. 2002, ApJL, 573, L137

Andreani, P., Cristiani, S., Grazian, A., La Franca, F., & Goldschmidt, P. 2003, AJ, 125, 444

Antonucci, R. R. J. & Miller, J. S. 1985, ApJ, 297, 621

Arav, N., Gabel, J. R., Korista, K. T., et al. 2007, ApJ, 658, 829

Arp, H. 1968, ApJ, 152, 633

Avni, Y. 1976, ApJ, 210, 642

Baade, W. & Minkowski, R. 1954, ApJ, 119, 206

Baldwin, J., Ferland, G., Korista, K., & Verner, D. 1995, ApJL, 455, L119

Baldwin, J. A. 1997, in ASP Conf. Ser., Vol. 113, IAU Colloq. 159, ed. B. M. Peterson, F.-Z. Cheng, & A. S. Wilson, 80

Barger, A. J., Cowie, L. L., Mushotzky, R. F., & Richards, E. A. 2001, AJ, 121, 662

Barth, A. J., Nguyen, M. L., Malkan, M. A., et al. 2011, ApJ, 732, 121

Baskin, A. & Laor, A. 2005, MNRAS, 356, 1029

Baskin, A., Laor, A., & Stern, J. 2013, MNRAS, 438, 604

Becker, R. H., White, R. L., & Helfand, D. J. 1995, ApJ, 450, 559

Bentz, M. C., Denney, K. D., Cackett, E. M., et al. 2006a, ApJ, 651, 775

Bentz, M. C., Denney, K. D., Cackett, E. M., et al. 2007, ApJ, 662, 205

Bentz, M. C., Denney, K. D., Grier, C. J., et al. 2013, ApJ, 767, 149

Bentz, M. C., Horne, K., Barth, A. J., et al. 2010, ApJL, 720, L46

Bentz, M. C., Peterson, B. M., Netzer, H., Pogge, R. W., & Vestergaard, M. 2009, ApJ, 697, 160

Bentz, M. C., Peterson, B. M., Pogge, R. W., & Vestergaard, M. 2009, ApJL, 694, L166

Bentz, M. C., Peterson, B. M., Pogge, R. W., Vestergaard, M., & Onken, C. A. 2006b, ApJ, 644, 133

Binney, J. & Tremaine, S. 1987, Galactic dynamics (Princeton University Press)

Blandford, R. D. & McKee, C. F. 1982, ApJ, 255, 419

Bonchi, A., La Franca, F., Melini, G., Bongiorno, A., & Fiore, F. 2013, MNRAS, 429, 1970

Boroson, T. A. & Green, R. F. 1992, ApJS, 80, 109

Boutsia, K., Leibundgut, B., Trevese, D., & Vagnetti, F. 2009, A&A, 497, 81

Boutsia, K., Leibundgut, B., Trevese, D., & Vagnetti, F. 2010, in ASP Conf. Ser., Vol. 424, 9th International Conference of the Hellenic Astronomical Society, ed. K. Tsinganos, D. Hatzidimitriou, & T. Matsakos, 277

Burtscher, L., Meisenheimer, K., Tristram, K. R. W., et al. 2013, A&A, 558, A149

Cappellari, M., Bacon, R., Bureau, M., et al. 2006, MNRAS, 366, 1126

Cardelli, J. A., Clayton, G. C., & Mathis, J. S. 1989, ApJ, 345, 245

Cattaneo, A., Faber, S. M., Binney, J., et al. 2009, Nature, 460, 213

Chiaberge, M., Macchetto, F. D., Sparks, W. B., Capetti, A., & Celotti, A. 2003, in ASP Conf. Ser., Vol. 290, Active Galactic Nuclei: From Central Engine to Host Galaxy, ed. S. Collin, F. Combes, & I. Shlosman, 331

Ciotti, L., Ostriker, J. P., & Proga, D. 2009, ApJ, 699, 89

Collin, S., Kawaguchi, T., Peterson, B. M., & Vestergaard, M. 2006, A&A, 456, 75

Comastri, A., Ranalli, P., Iwasawa, K., et al. 2011, A&A, 526, L9

Condon, J. J., Anderson, E., & Broderick, J. J. 1995, AJ, 109, 2318

Condon, J. J., Yin, Q. F., Thuan, T. X., & Boller, T. 1998, AJ, 116, 2682

Cowie, L. L., Barger, A. J., Hu, E. M., Capak, P., & Songaila, A. 2004, AJ, 127, 3137

Croton, D. J., Springel, V., White, S. D. M., et al. 2006, MNRAS, 365, 11

Daddi, E., Alexander, D. M., Dickinson, M., et al. 2007, ApJ, 670, 173

Dasyra, K. M., Tacconi, L. J., Davies, R. I., et al. 2007, ApJ, 657, 102

Denney, K. D., Bentz, M. C., Peterson, B. M., et al. 2006, ApJ, 653, 152

Denney, K. D., Peterson, B. M., Dietrich, M., Vestergaard, M., & Bentz, M. C. 2009, ApJ, 692, 246

Denney, K. D., Peterson, B. M., Pogge, R. W., et al. 2010, ApJ, 721, 715

Devereux, N., Willner, S. P., Ashby, M. L. N., Willmer, C. N. A., & Hriljac, P. 2009, ApJ, 702, 955

Di Matteo, T., Springel, V., & Hernquist, L. 2005, Nature, 433, 604

Dietrich, M., Peterson, B. M., Grier, C. J., et al. 2012, ApJ, 757, 53

Dimitrijević, M. S., Popović, L. Č., Kovačević, J., Dačić, M., & Ilić, D. 2007, MNRAS, 374, 1181

Doi, M., Tanaka, M., Fukugita, M., et al. 2010, AJ, 139, 1628

Down, E. J., Rawlings, S., Sivia, D. S., & Baker, J. C. 2010, MNRAS, 401, 633

Efron, B. & Tibshirani, R. J. 1994, An Introduction to the Bootstrap (Chapman & Hall/CRC)

Elitzur, M. 2008, NAR, 52, 274

Elitzur, M., Ho, L. C., & Trump, J. R. 2014, MNRAS, 438, 3340

Elitzur, M. & Shlosman, I. 2006, ApJL, 648, L101

Elvis, M. 2000, ApJ, 545, 63

Elvis, M. 2012, ArXiv:1201.5101

Elvis, M., Hao, H., Civano, F., et al. 2012, ApJ, 759, 6

Elvis, M., Schreier, E. J., Tonry, J., Davis, M., & Huchra, J. P. 1981, ApJ, 246, 20

Fabian, A. C., Iwasawa, K., Reynolds, C. S., & Young, A. J. 2000, PASP, 112, 1145

Fabian, A. C., Vaughan, S., Nandra, K., et al. 2002, MNRAS, 335, L1

Fabian, A. C., Zoghbi, A., Ross, R. R., et al. 2009, Nature, 459, 540

Fan, X., Strauss, M. A., Schneider, D. P., et al. 1999, in BAAS, Vol. 31, AAS Meeting Abstracts, 1517

Ferland, G. J., Hu, C., Wang, J., et al. 2009, ApJL, 707, L82

Ferland, G. J., Korista, K. T., Verner, D. A., et al. 1998, PASP, 110, 761

Ferland, G. J., Porter, R. L., van Hoof, P. A. M., et al. 2013, RMxAA, 49, 137

Ferrarese, L. & Ford, H. 2005, Space Sci. Rev., 116, 523

Ferrarese, L. & Merritt, D. 2000, ApJL, 539, L9

Feruglio, C., Daddi, E., Fiore, F., et al. 2011, ApJL, 729, L4

Filippenko, A. V. & Sargent, W. L. W. 1985, ApJS, 57, 503

Filippenko, A. V. & Terlevich, R. 1992, ApJL, 397, L79

Fine, S., Croom, S. M., Miller, L., et al. 2006, MNRAS, 373, 613

Fiore, F., La Franca, F., Vignali, C., et al. 2000, NA, 5, 143

Galavis, M. E., Mendoza, C., & Zeippen, C. J. 1997, A&AS, 123, 159

Gebhardt, K., Bender, R., Bower, G., et al. 2000a, ApJL, 539, L13

Gebhardt, K., Kormendy, J., Ho, L. C., et al. 2000b, ApJL, 543, L5

Genzel, R. & Cesarsky, C. J. 2000, ARA&A, 38, 761

Genzel, R., Eisenhauer, F., & Gillessen, S. 2010, Rev. Mod. Phys., 82, 3121

Giacconi, R., Rosati, P., Tozzi, P., et al. 2001, ApJ, 551, 624

Gibson, R. R., Jiang, L., Brandt, W. N., et al. 2009, ApJ, 692, 758

Gilli, R., Comastri, A., & Hasinger, G. 2007, A&A, 463, 79

Goad, M. R., Korista, K. T., & Ruff, A. J. 2013, MNRAS, 426, 3086

Goldschmidt, P., Kukula, M. J., Miller, L., & Dunlop, J. S. 1999, ApJ, 511, 612

Graham, A. W. 2008, ApJ, 680, 143

Graham, A. W., Driver, S. P., Allen, P. D., & Liske, J. 2007, MNRAS, 378, 198

Graham, A. W., Onken, C. A., Athanassoula, E., & Combes, F. 2011, MNRAS, 412, 2211

Graham, M. J., Djorgovski, S. G., Drake, A. J., et al. 2014, MNRAS, 439, 703

Granato, G. L., De Zotti, G., Silva, L., Bressan, A., & Danese, L. 2004, ApJ, 600, 580

Greene, J. E. & Ho, L. C. 2005, ApJ, 630, 122

Greene, J. E. & Ho, L. C. 2006, ApJL, 641, L21

Greene, J. E. & Ho, L. C. 2009, PASP, 121, 1167

Greenstein, J. L. 1963, Nature, 197, 1041

Grier, C. J., Martini, P., Watson, L. C., et al. 2013, ApJ, 773, 90

Grier, C. J., Peterson, B. M., Bentz, M. C., et al. 2008, ApJ, 688, 837

Grier, C. J., Peterson, B. M., Pogge, R. W., et al. 2012, ApJ, 755, 60

Gültekin, K., Richstone, D. O., Gebhardt, K., et al. 2009, ApJ, 698, 198

Gunn, J. E., Carr, M., Rockosi, C., et al. 1998, AJ, 116, 3040

Gunn, J. E., Siegmund, W. A., Mannery, E. J., et al. 2006, AJ, 131, 2332

Hamann, F. & Ferland, G. 1992, ApJL, 391, L53

Hao, H., Elvis, M., Civano, F., et al. 2010, ApJL, 724, L59

Hao, H., Elvis, M., Civano, F., & Lawrence, A. 2011, ApJ, 733, 108

Häring, N. & Rix, H.-W. 2004, ApJL, 604, L89

Harrison, C. M., Alexander, D. M., Swinbank, A. M., et al. 2012, MNRAS, 426, 1073

Heckman, T. M., Armus, L., McCarthy, P., van Breugel, W., & Miley, G. K. 1987, in NASACP, Vol. 2466, NASA Conf. Pub., ed. C. J. Lonsdale Persson, 461–469

Hewett, P. C. & Foltz, C. B. 1994, PASP, 106, 113

Hewett, P. C. & Foltz, C. B. 2003, AJ, 125, 1784

Ho, L. C., Filippenko, A. V., & Sargent, W. L. W. 2003, ApJ, 583, 159

Holweger, H. 2001, in AIP Conf. Ser., Vol. 598, Joint SOHO/ACE workshop, ed. R. F. Wimmer-Schweingruber, 23–30

Hönig, S. F. & Kishimoto, M. 2010, A&A, 523, A27

Hopkins, P. F., Murray, N., & Thompson, T. A. 2009, MNRAS, 398, 303

Hornschemeier, A. E., Bauer, F. E., Alexander, D. M., et al. 2003, Astron. Nachr., 324, 12

Hoyle, F. & Fowler, W. A. 1963, Nature, 197, 533

Hu, J. 2009, ArXiv:0908.2028

Ivezić,Ž ., Menou, K., Knapp, G. R., et al. 2002, AJ, 124, 2364

Iwasawa, K., Gilli, R., Vignali, C., et al. 2012a, A&A, 546, A84

Iwasawa, K., Mainieri, V., Brusa, M., et al. 2012b, A&A, 537, A86

Jaffe, W., Meisenheimer, K., Röttgering, H. J. A., et al. 2004, Nature, 429, 47

Jarvis, M. J. & McLure, R. J. 2006, MNRAS, 369, 182

Jiang, L., Fan, X., Brandt, W. N., et al. 2010, Nature, 464, 380

Jiang, L., Fan, X., Vestergaard, M., et al. 2007, AJ, 134, 1150

Jun, H. D. & Im, M. 2013, ApJ, 779, 104

Kaspi, S., Brandt, W. N., Maoz, D., et al. 2007, ApJ, 659, 997

Kaspi, S., Maoz, D., Netzer, H., et al. 2005, ApJ, 629, 61

Kaspi, S. & Netzer, H. 1999, ApJ, 524, 71

Kaspi, S., Smith, P. S., Netzer, H., et al. 2000, ApJ, 533, 631

Kellermann, K. I., Sramek, R., Schmidt, M., Shaffer, D. B., & Green, R. 1989, AJ, 98, 1195

Kishimoto, M., Hönig, S. F., Antonucci, R., et al. 2011, A&A, 536, A78

Knigge, C., Scaringi, S., Goad, M. R., & Cottis, C. E. 2008, MNRAS, 386, 1426

Kollgaard, R. I., Feigelson, E. D., Laurent-Muehleisen, S. A., et al. 1995, ApJ, 449, 61

Korista, K. T. & Goad, M. R. 2000, ApJ, 536, 284

Korista, K. T. & Goad, M. R. 2004, ApJ, 606, 749

Kormendy, J. & Bender, R. 2009, ApJL, 691, L142

Kormendy, J. & Ho, L. C. 2013a, ARA&A, 51, 511

Kormendy, J. & Ho, L. C. 2013b, ArXiv:1308.6483

Kormendy, J. & Kennicutt, Jr., R. C. 2004, ARA&A, 42, 603

Kormendy, J. & Richstone, D. 1995, ARA&A, 33, 581

Krause, M., Burkert, A., & Schartmann, M. 2011, MNRAS, 411, 550

Krolik, J. H. 2001, ApJ, 551, 72

Krolik, J. H., McKee, C. F., & Tarter, C. B. 1981, ApJ, 249, 422

Kuo, C. Y., Braatz, J. A., Condon, J. J., et al. 2011, ApJ, 727, 20

La Franca, F., Gregorini, L., Cristiani, S., de Ruiter, H., & Owen, F. 1994, AJ, 108, 1548

La Franca, F., Melini, G., & Fiore, F. 2010, ApJ, 718, 368

Lamastra, A., Menci, N., Maiolino, R., Fiore, F., & Merloni, A. 2010, MNRAS, 405, 29

Laor, A. 1998, ApJL, 505, L83

Laurent, O., Mirabel, I. F., Charmandaris, V., et al. 2000, A&A, 359, 887

Leisy, P. & Dennefeld, M. 1996, A&AS, 116, 95

Liebling, S. L. & Palenzuela, C. 2012, Living Rev. Relat., 15, 6

Lusso, E., Comastri, A., Simmons, B. D., et al. 2012, MNRAS, 425, 623

Lynden-Bell, D. 1969, Nature, 223, 690

Lynden-Bell, D. & Rees, M. J. 1971, MNRAS, 152, 461

MacLeod, C. L., Brooks, K., Ivezić,Ž ., et al. 2011, ApJ, 728, 26

Magorrian, J., Tremaine, S., Richstone, D., et al. 1998, AJ, 115, 2285

Maiolino, R., Gallerani, S., Neri, R., et al. 2012, MNRAS, 425, L66

Maiolino, R., Marconi, A., & Oliva, E. 2001, A&A, 365, 37

Maiolino, R., Risaliti, G., Salvati, M., et al. 2010, A&A, 517, A47

Mannucci, F., Salvati, M., & Stanga, R. M. 1992, ApJ, 394, 98

Marconi, A., Axon, D. J., Maiolino, R., et al. 2008, ApJ, 678, 693

Marconi, A., Axon, D. J., Maiolino, R., et al. 2009, ApJL, 698, L103

Marconi, A. & Hunt, L. K. 2003, ApJL, 589, L21

Marconi, A., Pastorini, G., Pacini, F., et al. 2006, A&A, 448, 921

Marconi, A., Risaliti, G., Gilli, R., et al. 2004, MNRAS, 351, 169

Markwardt, C. B. 2009, in ASP Conf. Ser., Vol. 411, Astronomical Data Analysis Software and Systems XVIII, ed. D. A. Bohlender, D. Durand, & P. Dowler, 251

Marulli, F., Bonoli, S., Branchini, E., Moscardini, L., & Springel, V. 2008, MNRAS, 385, 1846

Marziani, P., Sulentic, J. W., & Dultzin, D. 2008, in , 69–73

Marziani, P., Sulentic, J. W., Stirpe, G. M., Zamfir, S., & Calvani, M. 2009, A&A, 495, 83

Mathis, J. S., Rumpl, W., & Nordsieck, K. H. 1977, ApJ, 217, 425

McGill, K. L., Woo, J.-H., Treu, T., & Malkan, M. A. 2008, ApJ, 673, 703

McLure, R. J. & Dunlop, J. S. 2002, MNRAS, 331, 795

McLure, R. J. & Dunlop, J. S. 2004, MNRAS, 352, 1390

McLure, R. J. & Jarvis, M. J. 2002, MNRAS, 337, 109

Menci, N., Fiore, F., Puccetti, S., & Cavaliere, A. 2008, ApJ, 686, 219

Merloni, A. 2009, in AIP Conf. Ser., ed. S. Heinz & E. Wilcots, Vol. 1201, 108–114

Merloni, A. & Heinz, S. 2008, MNRAS, 388, 1011

Metzroth, K. G., Onken, C. A., & Peterson, B. M. 2006, ApJ, 647, 901

Miller, N. A. & Owen, F. N. 2001, AJ, 121, 1903

Miyoshi, M., Moran, J., Herrnstein, J., et al. 1995, Nature, 373, 127

Mor, R. & Netzer, H. 2012, MNRAS, 420, 526

Mor, R., Netzer, H., & Elitzur, M. 2009, ApJ, 705, 298

Mortlock, D. J., Warren, S. J., Venemans, B. P., et al. 2011, Nature, 474, 616

Mushotzky, R. 2004, in Ap&SSL, Vol. 308, Supermassive Black Holes in the Distant Universe, ed. A. J. Barger, 53

Mushotzky, R. F., Cowie, L. L., Barger, A. J., & Arnaud, K. A. 2000, Nature, 404, 459

Mushotzky, R. F. & Wandel, A. 1989, ApJ, 339, 674

Nagao, T., Marconi, A., & Maiolino, R. 2006, A&A, 447, 157

Nakamura, O., Fukugita, M., Yasuda, N., et al. 2003, AJ, 125, 1682

Nandra, K., George, I. M., Mushotzky, R. F., Turner, T. J., & Yaqoob, T. 1997, ApJ, 477, 602

Nandra, K., George, I. M., Mushotzky, R. F., Turner, T. J., & Yaqoob, T. 1999, ApJL, 523, L17

Nandra, K., George, I. M., Turner, T. J., & Fukazawa, Y. 1996, ApJ, 464, 165

Nandra, K., O'Neill, P. M., George, I. M., & Reeves, J. N. 2007, MNRAS, 382, 194

Nelson, C. H., Green, R. F., Bower, G., Gebhardt, K., & Weistrop, D. 2004, ApJ, 615, 652

Nenkova, M., Ivezić,Ž ., & Elitzur, M. 2002, ApJL, 570, L9

Nenkova, M., Sirocky, M. M., Ivezić,Ž ., & Elitzur, M. 2008, ApJ, 685, 147

Netzer, H. 1996, ApJ, 473, 781

Netzer, H. 2008, NAR, 52, 257

Netzer, H. 2009, ApJ, 695, 793

Netzer, H. & Laor, A. 1993, ApJL, 404, L51

Netzer, H., Laor, A., & Gondhalekar, P. M. 1992, MNRAS, 254, 15

Netzer, H., Lira, P., Trakhtenbrot, B., Shemmer, O., & Cury, I. 2007, ApJ, 671, 1256

Netzer, H. & Maoz, D. 1990, ApJL, 365, L5

Netzer, H. & Marziani, P. 2010, ApJ, 724, 318

Netzer, H. & Trakhtenbrot, B. 2013, MNRAS

Onken, C. A. 2009, ArXiv:0907.4192

Onken, C. A., Ferrarese, L., Merritt, D., et al. 2004, ApJ, 615, 645

Onken, C. A. & Kollmeier, J. A. 2008, ApJ, 689, L13

Onken, C. A. & Peterson, B. M. 2002, ApJ, 572, 746

Osterbrock, D. E. 1981, ApJ, 249, 462

Padovani, P. 1993, MNRAS, 263, 461

Pancoast, A., Brewer, B. J., & Treu, T. 2011, ApJ, 730, 139

Pancoast, A., Brewer, B. J., & Treu, T. 2014, MNRAS, 445, 3055

Pâris, I., Petitjean, P., Aubourg, É., et al. 2014, A&A, 563, A54

Park, D., Kelly, B. C., Woo, J.-H., & Treu, T. 2012, ApJS, 203, 6

Peebles, P. J. E. & Yu, J. T. 1970, ApJ, 162, 815

Peterson, B. M. 2004, in IAU Symposium, Vol. 222, The Interplay Among Black Holes, Stars and ISM in Galactic Nuclei, ed. T. Storchi-Bergmann, L. C. Ho, & H. R. Schmitt, 15–20

Peterson, B. M. 2011, ArXiv:1109.4181

Peterson, B. M. 2014, Space Sci. Rev., 183, 253

Peterson, B. M. & Bentz, M. C. 2011, Black-hole masses from reverberation mapping (Cambridge University Press), 100–111

Peterson, B. M., Bentz, M. C., Desroches, L.-B., et al. 2005, ApJ, 632, 799

Peterson, B. M., Ferrarese, L., Gilbert, K. M., et al. 2004, ApJ, 613, 682

Peterson, B. M., Grier, C. J., Horne, K., et al. 2014, ApJ, 795, 149

Peterson, B. M. & Wandel, A. 2000, ApJL, 540, L13

Proga, D. 2007, in ASP Conf. Ser., Vol. 373, The Central Engine of Active Galactic Nuclei, ed. L. C. Ho & J.-W. Wang, 267

Puchnarewicz, E. M., Mason, K. O., Romero-Colmenero, E., et al. 1996, MNRAS, 281, 1243

Raban, D., Jaffe, W., Röttgering, H., Meisenheimer, K., & Tristram, K. R. W. 2009, MNRAS, 394, 1325

Rees, M. J., Netzer, H., & Ferland, G. J. 1989, ApJ, 347, 640

Reichard, T. A., Richards, G. T., Hall, P. B., et al. 2003, AJ, 126, 2594

Richards, G. T., Fan, X., Newberg, H. J., et al. 2002, AJ, 123, 2945

Richards, G. T., Myers, A. D., Gray, A. G., et al. 2009, ApJS, 180, 67

Richards, G. T., Strauss, M. A., Croom, S. M., et al. 2004, in BAAS, Vol. 36, AAS Meeting Abstracts, 167.03

Risaliti, G. 2009, in Proc. Int. Astron. Union, Vol. 5, Co-Evolution of Central Black Holes and Galaxies, 299–306

Risaliti, G. & Elvis, M. 2004, in Ap&SSL, Vol. 308, Supermassive Black Holes in the Distant Universe, ed. A. J. Barger, 187

Risaliti, G., Elvis, M., Fabbiano, G., et al. 2007, ApJL, 659, L111

Risaliti, G., Elvis, M., & Nicastro, F. 2002, ApJ, 571, 234

Risaliti, G., Maiolino, R., Marconi, A., et al. 2003, ApJL, 595, L17

Risaliti, G., Miniutti, G., Elvis, M., et al. 2009a, ApJ, 696, 160

Risaliti, G., Salvati, M., Elvis, M., et al. 2009b, MNRAS, 393, L1

Risaliti, G., Salvati, M., & Marconi, A. 2011, MNRAS, 411, 2223

Rowan-Robinson, M. 1977, ApJ, 213, 635

Sadler, E. M., Jackson, C. A., Cannon, R. D., et al. 2002, MNRAS, 329, 227

Salpeter, E. E. 1964, ApJ, 140, 796

Salviander, S., Shields, G. A., Gebhardt, K., & Bonning, E. W. 2007, ApJ, 662, 131

Sandage, A. R. 1971, in Study Week on Nuclei of Galaxies, ed. D. J. K. O'Connell, 271

Sani, E., Marconi, A., Hunt, L. K., & Risaliti, G. 2011, MNRAS, 413, 1479

Sargent, W. L. W. 1970, ApJ, 160, 405

Scaringi, S., Cottis, C. E., Knigge, C., & Goad, M. R. 2009, MNRAS, 399, 2231

Schlegel, D. J., Finkbeiner, D. P., & Davis, M. 1998, ApJ, 500, 525

Schmidt, M. 1963, Nature, 197, 1040

Schmidt, M. 1969, in Quasars and high-energy astronomy, 55

Schmidt, M. & Matthews, T. A. 1964, ApJ, 139, 781

Schneider, D. P., Richards, G. T., Hall, P. B., et al. 2010, AJ, 139, 2360

Shankar, F., Weinberg, D. H., & Miralda-Escudé, J. 2013, MNRAS, 428, 421

Shen, Y. 2013, Bull. Astr. Soc. India, 41, 61

Shen, Y., Greene, J. E., Strauss, M. A., Richards, G. T., & Schneider, D. P. 2008, ApJ, 680, 169

Shen, Y., Richards, G. T., Strauss, M. A., et al. 2011, ApJS, 194, 45

Shen, Y., Strauss, M. A., Ross, N. P., et al. 2009, ApJ, 697, 1656

Silk, J. & Rees, M. J. 1998, A&A, 331, L1

Soltan, A. 1982, MNRAS, 200, 115

Spinoglio, L. & Malkan, M. A. 1989, ApJ, 342, 83

Spitzer, Jr., L. 1985, ApJL, 290, L21

Springel, V., White, S. D. M., Jenkins, A., et al. 2005, Nature, 435, 629

Storey, P. J. & Zeippen, C. J. 2000, MNRAS, 312, 813

Strateva, I. V., Brandt, W. N., Schneider, D. P., Vanden Berk, D. G., & Vignali, C. 2005, AJ, 130, 387

Suganuma, M., Yoshii, Y., Kobayashi, Y., et al. 2006, ApJ, 639, 46

Sulentic, J. W., Bachev, R., Marziani, P., Negrete, C. A., & Dultzin, D. 2007, ApJ, 666, 757

Sulentic, J. W., Repetto, P., Stirpe, G. M., et al. 2006, A&A, 456, 929

Sulentic, J. W., Zamfir, S., Marziani, P., & Dultzin, D. 2008, RMxAA, 32, 51

Sunyaev, R. A. & Zeldovich, Y. B. 1970, AP&SS, 7, 3

Tanaka, Y., Nandra, K., Fabian, A. C., et al. 1995, Nature, 375, 659

Tegmark, M., Strauss, M. A., Blanton, M. R., et al. 2004, Phys. Rev. D, 69, 103501

Telfer, R. C., Zheng, W., Kriss, G. A., & Davidsen, A. F. 2002, ApJ, 565, 773

Tombesi, F., Cappi, M., Reeves, J. N., & Braito, V. 2012, MNRAS, 422, L1

Torricelli-Ciamponi, G., Pietrini, P., Risaliti, G., & Salvati, M. 2014, MNRAS, 442, 2116

Tremaine, S., Gebhardt, K., Bender, R., et al. 2002, ApJ, 574, 740

Treu, T., Malkan, M. A., & Blandford, R. D. 2004, ApJL, 615, L97

Trevese, D., Perna, M., Vagnetti, F., Saturni, F. G., & Dadina, M. 2014, ApJ, 795, 164

Tristram, K. R. W., Meisenheimer, K., Jaffe, W., et al. 2007, A&A, 474, 837

Tsuzuki, Y., Kawara, K., Yoshii, Y., et al. 2006, ApJ, 650, 57

Urry, C. M. & Padovani, P. 1995, PASP, 107, 803

Urry, M. 2003, in ASP Conf. Ser., Vol. 290, Active Galactic Nuclei: From Central Engine to Host Galaxy, ed. S. Collin, F. Combes, & I. Shlosman, 3

van der Marel, R. P. 2004, Coevolution of Black Holes and Galaxies, 37

van der Marel, R. P. & Franx, M. 1993, ApJ, 407, 525

van Hoof, P. A. M., Weingartner, J. C., Martin, P. G., Volk, K., & Ferland, G. J. 2004, MNRAS, 350, 1330

Vanden Berk, D. E., Richards, G. T., Bauer, A., et al. 2001, AJ, 122, 549

Vasudevan, R. V. & Fabian, A. C. 2007, MNRAS, 381, 1235

Vaughan, S., Fabian, A. C., Iwasawa, K., & Turner, A. K. 2004, Nucl. Phys. B - Proc. Sup., 132, 244

Véron-Cetty, M.-P., Joly, M., & Véron, P. 2004, A&A, 417, 515

Vestergaard, M. 2002, ApJ, 571, 733

Vestergaard, M. 2004, ApJ, 601, 676

Vestergaard, M. & Osmer, P. S. 2009, ApJ, 699, 800

Vestergaard, M. & Peterson, B. M. 2006, ApJ, 641, 689

Vestergaard, M. & Wilkes, B. J. 2001, ApJS, 134, 1

Vignali, C., Brandt, W. N., & Schneider, D. P. 2003a, AJ, 125, 433

Vignali, C., Brandt, W. N., Schneider, D. P., Garmire, G. P., & Kaspi, S. 2003b, AJ, 125, 418

Vignali, C., Brandt, W. N., Schneider, D. P., & Kaspi, S. 2005, AJ, 129, 2519

Vignali, C., Mignoli, M., Gilli, R., et al. 2014, A&A, 571, A34

Wandel, A., Peterson, B. M., & Malkan, M. A. 1999, ApJ, 526, 579

Wang, J., Dong, X., Wang, T., et al. 2009, ApJ, 707, 1334

Watson, D., Denney, K. D., Vestergaard, M., & Davis, T. M. 2011, ApJL, 740, L49

Watson, L. C., Martini, P., Dasyra, K. M., et al. 2008, ApJL, 682, L21

Weymann, R. J., Morris, S. L., Foltz, C. B., & Hewett, P. C. 1991, ApJ, 373, 23

White, R. L., Becker, R. H., Gregg, M. D., et al. 2000, ApJS, 126, 133

Willott, C. J., McLure, R. J., & Jarvis, M. J. 2003, ApJL, 587, L15

Wilms, J., Reynolds, C. S., Begelman, M. C., et al. 2001, MNRAS, 328, L27

Woo, J. ., Treu, T., Malkan, M. A., & Blandford, R. 2008, ApJ, 681, 925

Woo, J., Treu, T., Barth, A. J., et al. 2010, ApJ, 716, 269

Wu, X.-B., Wang, R., Kong, M. Z., Liu, F. K., & Han, J. L. 2004, A&A, 424, 793

York, D. G., Adelman, J., Anderson, Jr., J. E., et al. 2000, AJ, 120, 1579

Yu, Q. & Tremaine, S. 2002, MNRAS, 335, 965

Yun, M. S., Reddy, N. A., & Condon, J. J. 2001, ApJ, 554, 803

Zel'dovich, Y. B. 1964, Sov. Phys. Dokl., 9, 195

Zheng, W. & Malkan, M. A. 1993, ApJ, 415, 517

Acknowledgements

I would like to express my gratitude to Prof. Alessandro Marconi for his unceasing support during all these years. I'm also very grateful to Prof. Hagai Netzer, Prof. Roberto Maiolino and Prof. Tohru Nagao for their useful collaboration and invaluable suggestions. Thanks also to the Arcetri Astrophysical Observatory and, in particular, to the Extragalactic Group for all the interesting meetings we had. And, finally, thanks to the Department of Physics and Astronomy for letting me start and complete this work.